Available online at www.sciencedirect.com
ScienceDirect
Geochimica et Cosmochimica Acta 75 (2011) 673–690
Geochimica et Cosmochimica Acta
www.elsevier.com/locate/gca

The effect of Si on metal–silicate partitioning of siderophile elements and implications for the conditions of core formation

James Tuff*, Bernard J. Wood, Jon Wade

Department of Earth Sciences, University of Oxford, South Parks Road, Oxford OX1 3AN, UK

Received 14 January 2010; accepted in revised form 29 October 2010; available online 9 November 2010

Abstract

We have determined the liquid metal–liquid silicate partitioning of Ni, Co, Mo, W, V, Cr and Nb at 1.5 GPa/1923 K and 6 GPa/2123 K under conditions of constant silicate melt composition with variable amounts of Si in the Fe-rich metallic liquid. Partitioning of Ni, Co, Mo, W and V is sensitive to the Si content of the metal with, in all five cases, increasing Si tending to make the element more lithophile than for conditions where the metal is Si-free. In contrast, metal–silicate partitioning of Cr and Nb is, at constant silicate melt composition, insensitive to the Si content of the metal.

The implications of our data are that if, as indicated by the Si isotopic composition of the silicate Earth (Georg et al., 2007; Fitoussi et al., 2009), the core contains significant amounts of Si, the important siderophile elements Ni, Co, W and Mo were more lithophile during accretion and core formation than previously believed.

We use our new data in conjunction with published metal–silicate partitioning results to develop a model of continuous accretion and core segregation taking explicit account of the partitioning of Si (this study) and O (from Ozawa et al., 2008) between metal and silicate and their effects on metal–silicate partitioning of siderophile elements. We find that the effect of Si on the siderophile characteristics of Ni, Co and W means that the pressures of core segregation estimated from these elements are ~5 GPa lower than those derived from experiments in which the metal contained negligible Si (e.g., Wade and Wood, 2005). The core–mantle partitioning of Cr and Nb requires that most of Earth accretion took place under conditions which were much more reducing than those implied by the current FeO content of the mantle and that the oxidation took place late in the accretionary process. Paths of terrestrial accretion, oxidation state and partitioning which are consistent with the current mantle contents of Ni, Co, W, V, Cr and Nb lead to Si and O contents of the core of ~4.3 wt.% and 0.15%, respectively.

1. INTRODUCTION

The accretion of the Earth was marked by segregation of most of the core within about 30 Myr (Kleine et al., 2002; Yin et al., 2002) and formation of the Moon by giant impact 70–110 Myr (Touboul et al., 2007; Halliday and Wood, 2009) after the origin of the solar system. Radiogenic isotopes (Kleine et al., 2002; Yin et al., 2002) provide information on the timing of these events while dynamical modelling yields general insight into the physics of planetary formation (Canup, 2004). More precise information on the conditions of core formation depends primarily on knowledge of how siderophile elements such as Ni, Co and W partitioned themselves between the core and mantle during metal segregation. A first order observation, based on the composition of the mantle (Thibault and Walter, 1995; Li and Agee, 1996; Righter, 2003; Wade and Wood, 2005) is that pressures appear to have been high (~40 GPa) during the later stages of the process. These extreme conditions were accompanied by dissolution of about

* Corresponding author. Tel.: +44 (0)1865 272000.
E-mail address: James.Tuff@earth.ox.ac.uk (J. Tuff).

0016-7037/$ - see front matter © 2010 Elsevier Ltd. All rights reserved.
doi:10.1016/j.gca.2010.10.027

10% of one or more "light" elements in the metallic core (Birch, 1952). Although the identity of the latter is unconstrained by seismological and elasticity data, geochemical arguments in favour of H (Okuchi, 1997), C (Wood, 1993), O (Rubie et al., 2004), S (Brett, 1984) and Si (Ringwood, 1966) have been made at various times.

As the Earth accreted and the core segregated, all elements were distributed between the Fe-rich metallic phase and the silicate mantle according to their partition coefficients D_i defined as follows:

$$D_i = \frac{[i]_{\text{metal}}}{[i]_{\text{silicate}}} \quad (1)$$

where $[i]$ is the concentration of element I in the phase of interest. Elements with high values of D (siderophile) were strongly depleted in the silicate mantle while those with low D values (lithophile) were concentrated in the mantle. The observation that the silicate Earth has approximately the same ratios of refractory lithophile elements as chondritic meteorites (Allègre et al., 1995; McDonough and Sun, 1995) implies that all refractory elements are present in the bulk Earth (core plus mantle) in approximately chondritic proportions. This enables estimation of the core–mantle partition coefficients for refractory siderophile elements such as Fe, Ni, Co, W and the weakly siderophile elements V, Cr and Nb (Wade and Wood, 2005; Wood et al., 2008). These are given in Table 1. In principle these core–mantle values may be used to estimate conditions of core formation because metal–silicate partitioning depends on pressure, temperature, oxygen fugacity (fO_2) and the compositions of metal and silicate phases. The most obvious dependence is on fO_2, since transfer of an element (M) of valence n from silicate to metal involves reduction:

$$MO_{n/2} = M + \frac{n}{4}O_2 \quad (2)$$

Applying the current concentration of FeO in the mantle of about 8 wt.% and of Fe in the core of 80% (Allègre et al., 1995; McDonough and Sun, 1995), Reaction (2) yields an apparent fO_2 of core segregation approximately 2 log fO_2 units below Fe–FeO (iron–wüstite, IW) equilibrium. At this fO_2, high pressure experiments have demonstrated that the partition coefficients of some siderophile elements (notably Ni, Co, W) decrease as pressure increases (Li and Agee, 2001; Cottrell et al., 2009) while others such as Cr (Wood et al., 2008) exhibit little pressure-dependence of their siderophile character. By combining the pressure and temperature dependences of partitioning behaviour for a number of elements one can calculate, for fixed mantle composition, a pressure and temperature at which the core and mantle would, at equilibrium, generate the partition coefficients of Table 1. The result, at the current composition of the mantle, is a pressure of about 40 GPa and temperature of ~4000 K (Gessmann and Rubie, 2000; Chabot and Agee, 2003; Wade and Wood, 2005). The observation that high pressures are needed to explain core–mantle partitioning led to the 'deep magma ocean' hypothesis which, at its simplest, is interpreted as core–mantle equilibration at a single pressure, temperature and mantle composition. In this interpretation (Li and Agee, 1996; Righter and Drake, 1997), droplets of metallic liquid descended through a 700 km deep magma ocean, equilibrating with the silicate liquid as they fell (Rubie et al., 2003). The liquid metal ponded at the base of the magma ocean and subsequently descended in large diapirs to the growing core without further equilibration with the surrounding silicate. Wade and Wood (2005) extended this model by taking account of the fact that, since small asteroids and planets such as Mars have cores, the Earth almost certainly had a core when it was a Mars-sized body. The core must, therefore have segregated continuously during accretion with concomitant increases in pressure and temperature as the planet grew. The same kind of model is used to calculate the apparent mean-life of Earth accretion from W-isotope data (Yin et al., 2002; Kleine et al., 2004). In order to develop a physically realistic model of the magma ocean on the growing Earth, Wade and Wood (2005) argued that the base of the magma ocean must have remained at a temperature close to the liquidus (probably between solidus and liquidus) of the mantle silicate. This fixed point allows for the strong viscosity contrast between the liquid upper part of the mantle and the solid lower mantle above which the metal would have ponded. Applying this constraint and using experimental data for the refractory elements V, Ni, Co and W, Wade and Wood found that the estimated core–mantle partitioning values could only be matched if the Earth became about 2 log fO_2 units more oxidised as it accreted. This progressive oxidation would be consistent with a magma ocean, which averaged about 30% of mantle depth and a mean temperature of core segregation slightly below 3000 K. Furthermore, the implication of the reduced nature of much of accretion was that Si would have been a major component of the "light" element in the core.

Table 1
Partition coefficients consistent with core–mantle equilibration.

Element	McDonough and Sun (1995) and McDonough (2003)	Allègre et al. (1995)	Likely range
D_V	1.83	—	1.5–2.2
D_{Fe}	13.66	13.65	13.65
D_{Si}	0.29	0.34	0.1–0.35[a]
D_{Cr}	3.4	2.9	2.0–4.0[a]
D_{Co}	23.8	24.7	23–27
D_{Ni}	26.5	24.4	23–27
D_{Nb}	—	—	0–0.8
D_W	16	—	15–25
D_{Mo}	100	—	60–140

[a] Value uncertain due to volatility.

Recent isotopic measurements (Georg et al., 2007) have shown that the silicate Earth and the Moon have slightly higher $^{30}Si/^{28}Si$ ratios than silicate meteorites, including those from Mars. The most plausible explanation of this observation is that a few % of Si was partitioned into Earth's core as it segregated from the mantle, leaving a slight enrichment of the latter in ^{30}Si (Georg et al., 2007; Fitoussi et al., 2009). The similarity of Si isotopes in the mantles of the Earth and Moon may then be explained by isotopic equilibration of the two bodies after the

Moon-forming impact (Pahlevan and Stevenson, 2007). Metallurgical data indicate that dissolution of even small amounts of Si in liquid Fe can have profound effects on the activities of some trace components, notably of Mo (Ono-Nakazato et al., 2007), which means that significant partitioning of Si into the core of the growing Earth should have affected the observed minor element composition of the mantle. This in turn will change the estimated pressure–temperature–fO_2 conditions of accretion and core formation. In order to quantify the effects of Si dissolution in liquid Fe on metal–silicate partitioning of siderophile elements we have performed an experimental study in which our samples contained small amounts of Ni, Co, V, Cr, Nb, Mo and W in addition to Si-bearing liquid iron.

2. EXPERIMENTAL AND ANALYTICAL PROCEDURES

2.1. Experimental

Experimental pressure and temperature conditions and compositions of the starting materials are shown in Table 2. All starting materials were based on a mix of ~50% Fe metal and 50% silicate, the latter approximating the 1.5 GPa eutectic composition in the system anorthite–diopside–forsterite ($An_{50}Di_{28}Fo_{22}$; Presnall et al., 1978). In all experiments, the silicate portion was doped with a trace element mix containing combinations of Mo, Nb, W, Cr, and V as oxides. NiO and CoO were added to the metal portion and Si was added in varying amounts as $FeSi_2$. In order to assess any possible effect on the metal–silicate partitioning of these elements when starting with metal or oxide species, additional experiments used Mo, Ni and Co added as metals (see below). High purity oxide and metal powders were used throughout to make the starting compositions. The starting materials were ground under acetone to ensure fine grain size and homogeneity, before being dried prior to the experiment.

Experiments were performed at 1.5 and 6 GPa, using an end-loaded Boyd–England-type piston-cylinder apparatus and a Walker-type multi-anvil apparatus (Walker et al., 1990), respectively. All 1.5 GPa experiments used a ½-inch $BaCO_3$–SiO_2 glass assembly with a graphite heater (e.g., McDade et al., 2002). The internal spacers consisted of MgO that had been fired at 1000 °C to ensure dryness. 1.5 GPa experiments used MgO and SiO_2 capsules (see below). Pressures were calibrated using the 1.6 GPa reaction: $Ab = Jd + Qz$ at 600 °C (Holland, 1980), the 2.97 GPa quartz-coesite transition at 1000 °C (Bohlen and Boettcher, 1982) and the alumina content of enstatite co-existing with garnet in the MgO–Al_2O_3–SiO_2 system at 3 GPa and 1600 °C (McDade et al., 2002). A friction correction of −12% was thus applied (McDade et al., 2002).

The 6 GPa experiments employed octahedra made from castable MgO-based ceramic (Ceramacast 584, Aremco Products Inc.; Walker, 1991) with 18 mm edges and tungsten carbide anvils with 12 mm truncations. Internal spacers and capsules were made from MgO. The furnace assembly consisted of straight graphite heaters surrounded by outer sleeves of ZrO_2. All assembly parts, apart from the heater, were fired at 1000 °C for several hours prior to assembly. Pressure was calibrated at room temperature using transformations of Bi (I–II and II–V) and at 1200 °C using the transition of Fe_2SiO_4 in olivine to spinel (Yagi et al., 1987).

All temperatures were measured using $W_{95}Re_5$–$W_{74}Re_{26}$ thermocouples, with temperatures of 1650 and 1850 °C chosen to ensure melting of both the silicate and metal portions of the charges at 1.5 and 6 GPa, respectively. Piston cylinder experimental run times ranged from 2 min to over 2 h, in order to assess the effect of run durations on the trace element partitioning (Fig. 1). All multi-anvil experiments were run for ~5 min. These are normally sufficient to achieve equilibrium (Thibault and Walter, 1995; Corgne et al., 2008). All piston cylinder and multi-anvil experiments were quenched after the desired duration by turning off the power to the graphite heaters while maintaining run pressure, which was subsequently slowly released.

2.2. Major and trace element analysis

Recovered experimental products were sectioned longitudinally and mounted in acrylic before polishing. The metal invariably segregated into one or more large (>300 μm diameter) blobs surrounded by quenched liquid in the form of a mixture of glass and elongated quench crystals (Fig. 2), or glass in the case of the SiO_2 capsule experiments. The product phases were analysed using a JEOL JXA8800 electron microprobe. WDS analyses were conducted using a 20 kV accelerating voltage and 40–60 nA beam current with a 10 μm spot to improve averaging of glass and quench phases. At least 25 repeat analyses were collected for the silicate and metal portions in each charge, with care being taken to avoid any possible secondary fluorescence arising from analyses that were too close to the edge of each phase (Chabot and Drake, 1999). Counting times were as follows: 30 s peak and 15 s background for major elements (e.g., Si, Al, Ca, Mg, Fe); 60 s peak and 30 s background for elements used as internal standards during laser ablation ICP–MS (LA-ICP–MS) (e.g., Ni, Co, Mo, W). A range of synthetic and natural standards was used for calibration.

Trace-element concentrations of the co-existing silicate and metal melts were determined on run charges by LA-ICP–MS using a Perkin Elmer Elan DRCII quadrupole coupled with a New Wave Research UP213 Nd:YAG laser at the University of Cambridge. Beam diameters of 60 μm were used. The following masses were counted: ^{29}Si, ^{51}V,^{53}Cr, ^{57}Fe, ^{59}Co, ^{60}Ni, ^{93}Nb, ^{95}Mo, ^{182}W with yields calibrated on NIST 610 glass standard as the external standard. USGS glass standard BCR-2G was used as a secondary standard to monitor the accuracy of the calibration. Internal standards for silicate and metal were the Si and Fe contents of the two phases, which had been measured by electron microprobe. Metal analyses were checked by comparison of LA-ICP–MS concentrations for Ni, Co, Mo and W with those obtained by electron microprobe (Fig. 3). Background counts were monitored for the first 20 s of each 60-second analysis and were minimised by including a 60-second 'wash-out' between each collection. Raw counts were collected on the ICP–MS in peak-hopping

Table 2
Experimental run conditions.

Run	Starting composition[a]	Press. (GPa)	Temp. (°C)	Duration (min)
0935	$Fe_{55}(FeSi_2)_{45}$ + 8% Ni + 5% CoO	1.5	1650	40
0936	$Fe_{70}(FeSi_2)_{30}$ + 5% Ni + 6% CoO	1.5	1650	25
BW1007	$Fe_{80}(FeSi_2)_{20}$ + 10% MoO_3	1.5	1650	40
BW1008	$Fe_{90}(FeSi_2)_{10}$ + 10% MoO_3	1.5	1650	42
BW1009	$Fe_{70}(FeSi_2)_{30}$ + 10% MoO_3	1.5	1650	44
BW1015	$Fe_{90}(FeSi_2)_{10}$ + 7% Mo	1.5	1650	45
BW1025	Feg0(FeSi2)20 + 9% Co	1.5	1650	57
BW1026	$Fe_{80}(FeSi_2)_{20}$ + 4.5% Co	1.5	1650	25
BW1027	Fe + 2% Si + 15% Ni	1.5	1650	40
BW1028	$Fe_{80}(FeSi_2)_{20}$ + 8% Co	1.5	1650	15
BW1029	$Fe_{80}(FeSi_2)_{20}$ + 8% Co	1.5	1650	5
BW1030	Fe + 9% Ni	1.5	1650	50
BW1031	Fe + 9% Ni + 3% FeO	1.5	1650	45
BW1032	$Fe_{80}(FeSi_2)_{20}$ + 6% NiO + 8% Co	1.5	1650	45
BW1033	$Fe_{80}(FeSi_2)_{20}$ + 6% NiO + 8% Co	1.5	1650	15
BW1034	$Fe_{70}(FeSi_2)_{30}$ + 7% NiO + 7% Co	1.5	1650	50
BW1035	$Fe_{70}(FeSi_2)_{30}$ + 7% NiO + 7% Co	1.5	1650	15
BW1037	$Fe_{70}(FeSi_2)_{30}$ + 7% NiO + 7% Co	1.5	1650	62
BW1038	$Fe_{80}(FeSi_2)_{20}$ + 6% NiO + 8% Co	1.5	1650	60
BW1039	$Fe_{70}(FeSi_2)_{30}$ + 10% Ni + 10% Mo	1.5	1650	70
BW1041	$Fe_{55}(FeSi_2)_{45}$ + 6% Ni + 5% CoO	1.5	1650	20
BW1042	$Fe_{55}(FeSi_2)_{45}$ + 6% Ni + 5% CoO	1.5	1650	50
BW1043	$Fe_{55}(FeSi_2)_{45}$ + 6% Ni + 5% CoO	1.5	1650	5
BW1044	$Fe_{55}(FeSi_2)_{45}$ + 6% Ni + 5% CoO	1.5	1650	135
BW1045[b]	$Fe_{70}(FeSi_2)_{30}$ + Ni, CoO, Mo, (W, V, Cr oxides)	1.5	1650	28
BW1046	Fe + Ni, CoO, Mo, (W, V, Cr oxides)	1.5	1650	42
BW1047	$Fe_{55}(FeSi_2)_{45}$ + Ni, CoO, Mo, (W, V, Cr ox)	1.5	1650	33
BW1048	$Fe_{80}(FeSi_2)_{20}$ + Ni, CoO, Mo, (W, V, Cr ox)	1.5	1650	35
BW1049	$Fe_{70}(FeSi_2)_{30}$ + Ni, CoO, Mo, (W, V, Cr ox)	1.5	1650	10
BW1050	Fe70($FeSi_2$)30 + Ni, CoO, Mo, (W, V, Cr ox)	1.5	1650	2
BW1052	$Fe_{70}(FeSi_2)_{30}$ + Ni, CoO, Mo, (W, V, Cr ox)	1.5	1650	42
JT1002	$Fe_{94}Ni_6$[c]	1.5	1650	60
JT1008	$Fe_{94}Ni_6$ + 20% $FeSi_2$	1.5	1650	60
JT1011	$Fe_{80}(FeSi_2)_{20}$ + 8.3% NiO + 4.1% CoO	1.5	1650	60
JT1012	$Fe_{90}(FeSi_2)_{10}$ + 5% Ni + 5% CoO	1.5	1650	60
JT1014	Fe + 7% Ni	1.5	1650	60
JT1015	Fe + 4% Si + 7% Ni	1.5	1650	60
JW1053	$Fe_{70}(FeSi_2)_{30}$ + Ni + CoO	1.5	1650	20
JW1054	$Fe_{70}(FeSi_2)_{30}$ + Ni + CoO	1.5	1650	5
JW1055	$Fe_{70}(FeSi_2)_{30}$ + Ni + CoO	1.5	1650	45
JW1056	$Fe_{70}(FeSi_2)_{30}$ + Ni + CoO	1.5	1650	120
C8	$Fe_{94}Ni_6$	6.0	1850	5
C11	$Fe_{80}(FeSi_2)_{20}$ + 8.3% NiO + 4.1% CoO	6.0	1850	5
C12	$Fe_{70}(FeSi_2)_{30}$ + 5.6% Ni + 4.7% CoO	6.0	1850	5
C17	$Fe_{90}(FeSi_2)_{10}$ + 5% Ni + 5% CoO	6.0	1850	5
C18	$Fe_{94}Ni_6$ + 5% CoO	6.0	1850	5
C19	$Fe_{94}Ni_6$ + 5% CoO	6.0	1850	5
C20	$Fe_{94}Ni_6$ + 5% CoO	6.0	1850	5
C21	$Fe_{94}Ni_6$ + 5% CoO	6.0	1850	5
C22	$Fe_{55}(FeSi_2)_{45}$ + 8.3% NiO + 4.4% CoO	6.0	1850	5
C54	$Fe_{80}(FeSi_2)_{20}$ + 8% Co	6.0	1850	15
C56	$Fe_{80}(FeSi_2)_{20}$ + 8% Co	6.0	1850	5

[a] Starting compositions consist of approximately 50% (by weight) of the silicate ($Di_{28}Fo_{22}An_{50}$) portion, doped with trace elements, with the remainder based on Fe metal with additions of Ni, Co and/or $FeSi_2$.
[b] Experiments BW1045 to BW1052 used SiO_2 capsules. All other runs used MgO capsules.
[c] Fe:Ni ratios are fixed, based on values from McDonough and Sun (1995).

mode and displayed in time-resolved format. This allowed each ablation to be monitored to identify heterogeneities such as small metal inclusions in the silicate and compositional variations with depth. All silicate analyses that exhibited evidence of metal contamination (through spikes in siderophile Mo, W and Ni concentrations) were discarded.

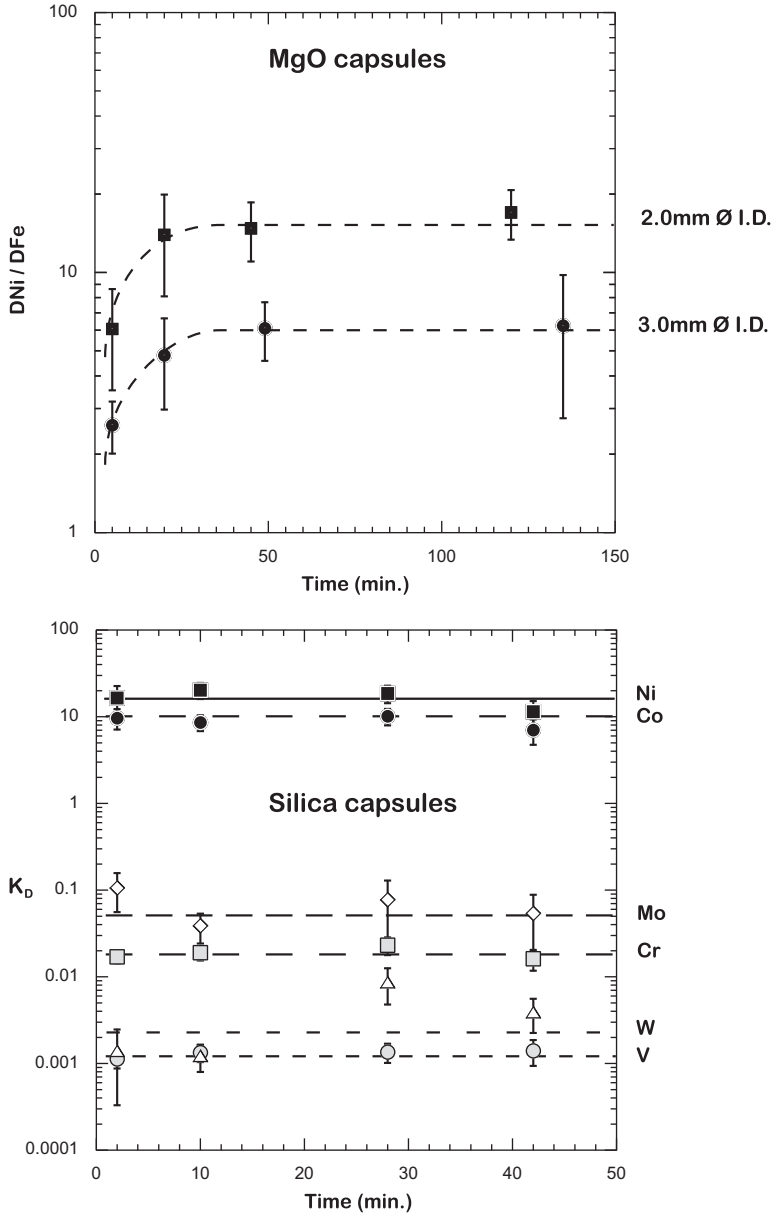

Fig. 1. Time-series experiments conducted to assess the run duration required in order to approach equilibrium, illustrated here as $K_D^{(\text{metal–silicate})}$ values plotted against run time. Error bars are propagated from the standard deviations of repeat analyses of metal and silicate in each run. The upper graph shows K_D (i.e., D_{Ni}/D_{Fe}) values for experiments in MgO capsules using two internal diameters (i.e., larger and smaller sample sizes). The lower graph shows K_D values for experiments in small sample (1.2 mm I.D.) SiO_2 capsules. Multi-anvil runs were conducted in MgO capsules, but with a similar I.D. (1.5 mm I.D.) and should have attained equilibrium within a similar time ($\leqslant$3 min).

Data reduction used the GLITTER (www.es.mq.edu.au/gemoc/glitter) software package.

2.3. Attainment of equilibrium and issues with Co in MgO capsules

Two sets of time series experiments were conducted in MgO capsules in order to assess the attainment of equilibrium during the runs. Experimental runs BW1041, 1042, 1043, 1044 (3.0 mm internal diameter capsules) and JW1053, 1054, 1055,1056, (2.0 mm internal diameter capsules) were doped with Ni and Co and run between 5 min to over 2 h. As can be seen in Fig. 1, the experiments conducted in 2.0 mm diameter and 3.0 mm internal diameter MgO capsules appear to approach equilibrium within ~15 min. In general, therefore, our experimental durations were much longer than this, 40–60 min. The multi-anvil runs at 6 GPa were conducted in smaller internal diameter capsules (1.5 mm I.D. and 1.5 mm length), and based on a time series in small diameter silica capsules (see below), should have approached equilibrium within 3 min.

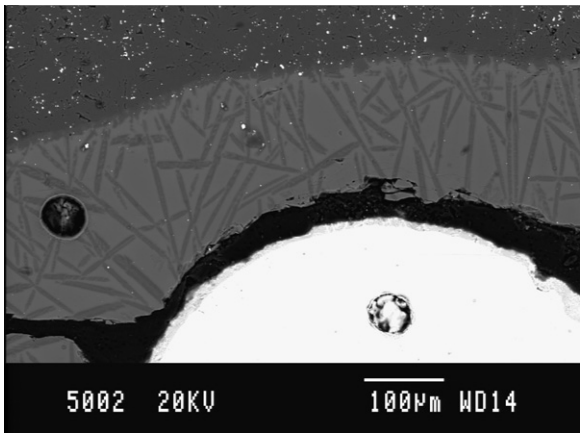

Fig. 2. Back-scattered electron image of experiment 0936. Upper dark region is the MgO capsule, which adjoins the quenched silicate melt. Note the feathery quench crystals distributed throughout the silicate glass. Bright region is a segregated metal ball. Circular pits were produced during LA-ICP–MS analysis.

Experiments were also conducted to assess whether starting with Ni, Co and Mo as oxides, as opposed to metals, affected their partitioning behaviour. Experiments conducted with oxides and metals, in both 1.5 and 6 GPa experiments, display the same partitioning behaviour (Figs. 4 and 5), verifying the conclusion that equilibrium had been approached in the experiments.

The behaviour of Co in experiments conducted in MgO capsules deserves special mention; it appears that Co in the silicate portion of each experimental charge is lost over the course of the experiment to the surrounding MgO. This results in large D_{Co}/D_{Fe} values, as there is virtually no measurable Co left in the silicate after each run. To counter this problem, we conducted experiments in SiO_2 glass capsules (1.2 mm I.D.) since Co should have low solubility in crystalline SiO_2. These experiments appear to approach equilibrium for all elements within 2 min. (Fig. 1). No evidence of Co loss was observed, and for Ni and Cr there is excellent in partitioning with data for MgO capsules. Because of the loss of Co from the charge to the capsule, the Co data from the MgO capsule runs at 1.5 GPa were discarded.

3. RESULTS

Major and trace element compositions of metal and silicate phases from experimental products are presented in Tables 3 and 4. When experiments were performed in MgO capsules, the silicate melt quenched to a mixture of glass and quench crystals (Fig. 1) with, as a result of MgO dissolution from the capsule, high MgO concentrations. Conversely, experiments performed in SiO_2 capsules contained quenched melt present as glass, with high SiO_2 contents (Table 3). Some elements (such as Ni and Co in the metal phase) were analysed by both electron microprobe and LA-ICP–MS (Tables 3 and 4). As Fig. 3 shows, the two methods are generally in excellent agreement. When microprobe and LA-ICP–MS data were both available, we used the electron microprobe values if the element in question was present at above 1000 ppm concentration. Figs. 4 and 5 show the results of our experiments at 1.5 and 6 GPa. We have plotted metal–silicate partitioning as a function of the Si content of the metal by ratioing to the partitioning of Fe in the same experiment. The reasoning for this is as follows. Metal–silicate partitioning of an element M involves exchange between oxidised M in the silicate and reduced M in the metal which must depend on oxygen fugacity and the oxidation state of M in the silicate, n (Reaction (2)):

$$\underset{\text{silicate}}{MO_{n/2}} = \underset{\text{metal}}{M} + \frac{n}{4}O_2$$

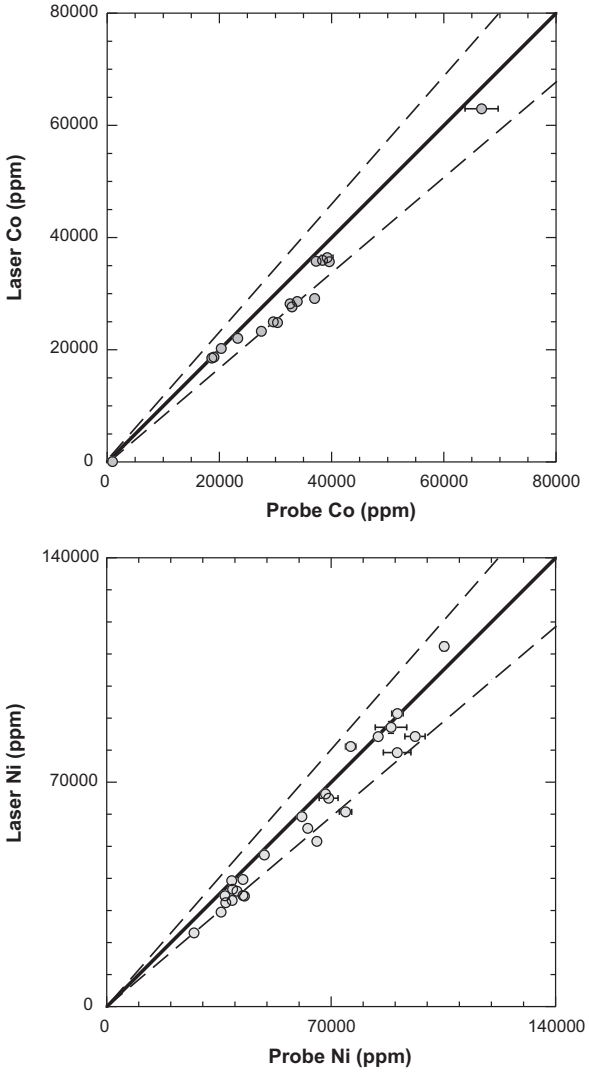

Fig. 3. Comparison of Co and Ni contents obtained by electron microprobe and LA-ICP–MS analyses on the same metal phases in our experimental run charges. Error bars are 1 standard deviation calculated and are from Tables 3 and 4. The solid lines represent a 1:1 ratio of laser and probe analysis (i.e., complete agreement). Nearly all of the data show good agreement between each method, with most data falling within 15% of the 1:1 line (shown as dashed lines).

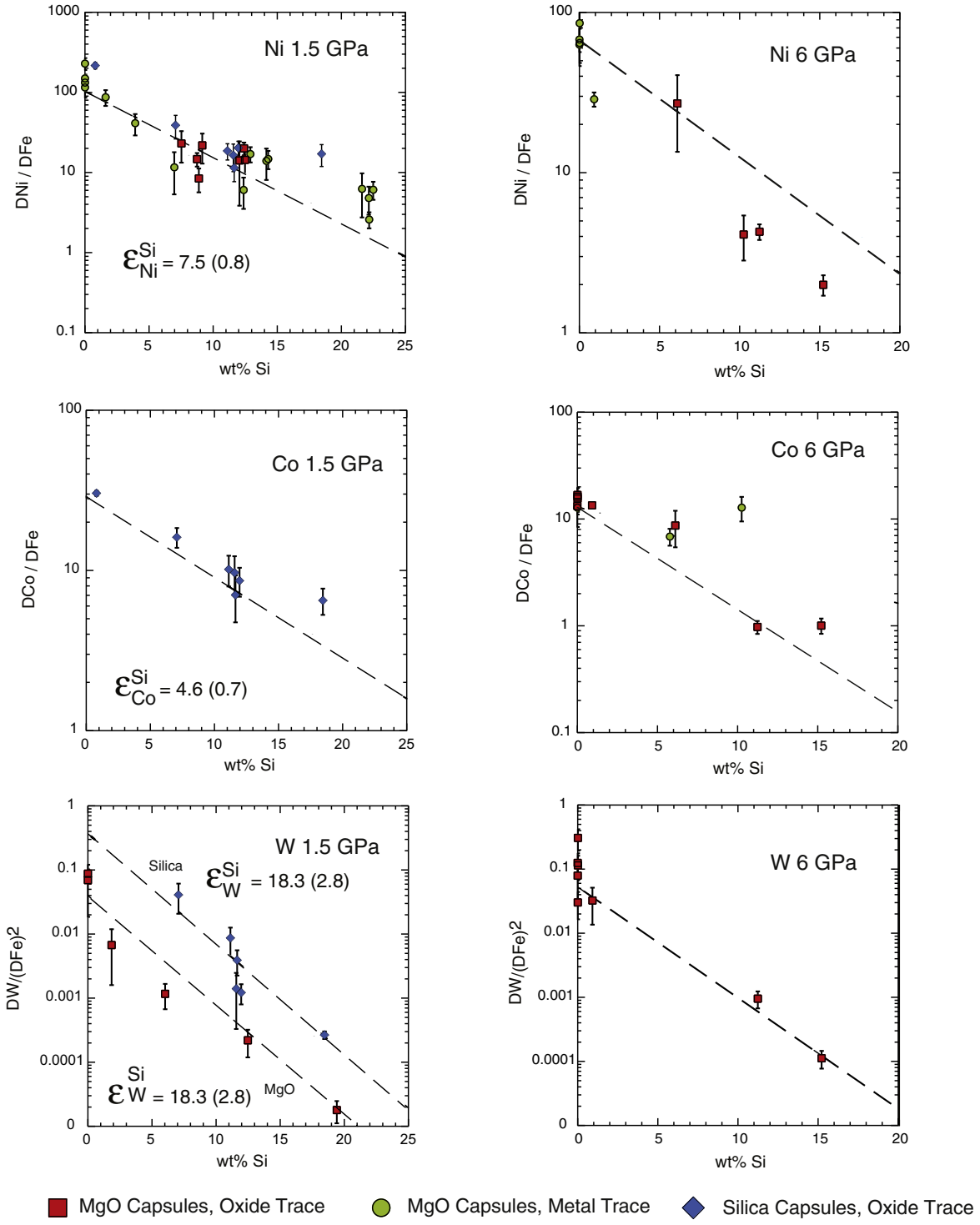

Fig. 4. $K_D^{(\text{metal–silicate})}$ values plotted versus metal Si content (in wt.%) for Ni, Co and W from experiments at 1.5 and 6 GPa. Data are from Tables 3 and 4. Error bars (shown where larger than symbols) were calculated, using error propagation, from the standard deviations in Tables 3 and 4. Data symbols are as follows: squares, MgO capsule runs with the element of interest added as an oxide; circles, MgO capsule runs with the element of interest added as a metal; diamonds, SiO_2 capsule runs (Table 2). ε_i^{Si} values were obtained by regressing K_D vs. Si for each element (dashed lines) and solving for epsilon using the epsilon-model of non-ideal interactions in Fe liquids (see text and Table 5). Numbers in parentheses are 1 standard error.

Therefore the metal–silicate partition coefficient of M depends on oxygen fugacity as well as pressure, temperature and the compositions of metal and silicate phases. We eliminated pressure, temperature and silicate composition as

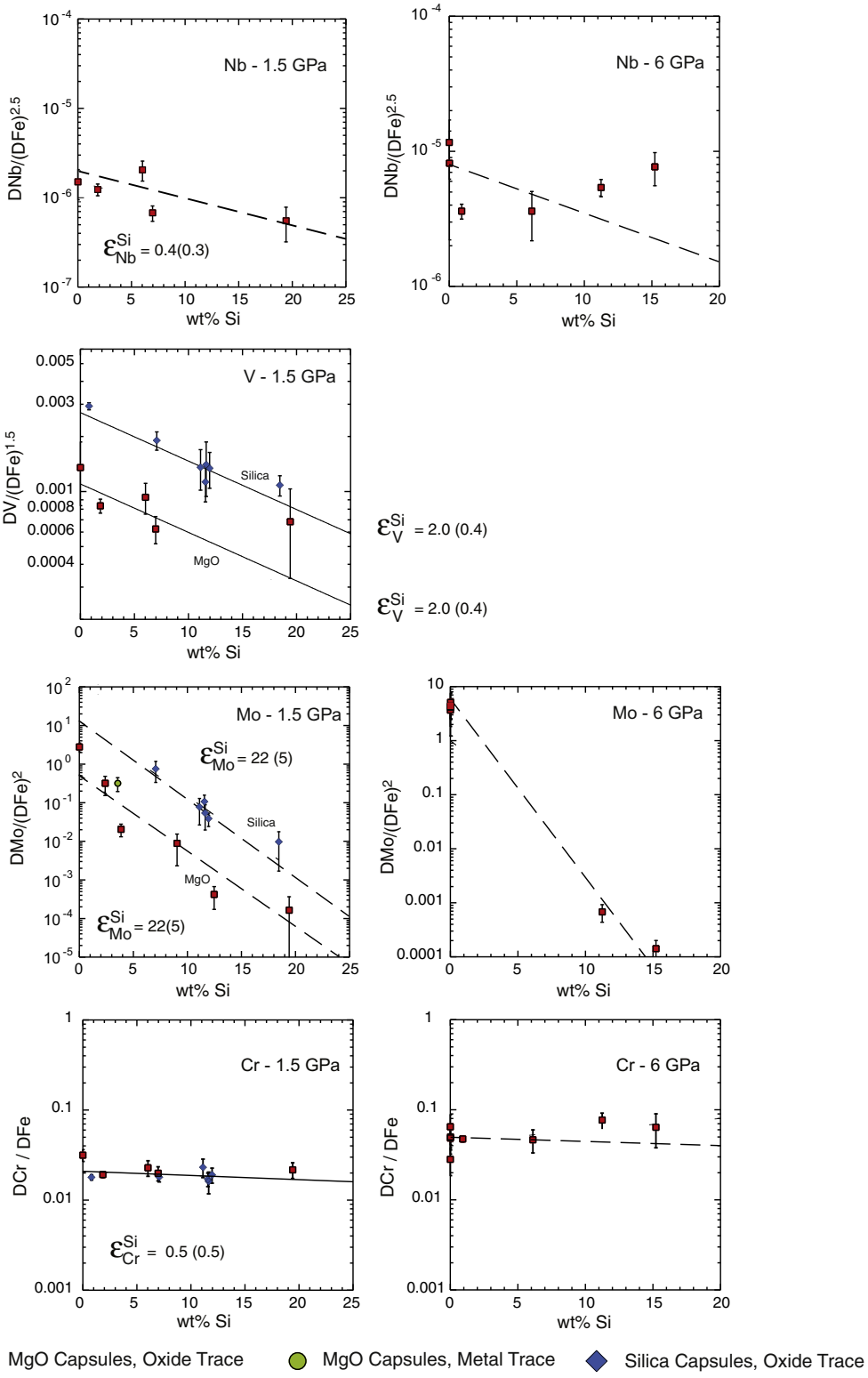

Fig. 5. $K_D^{(\text{metal–silicate})}$ values plotted versus metal Si content (in wt.%) for Nb, V, Mo and Cr from experiments at 1.5 and 6 GPa. Data are from Tables 3 and 4. Error bars (shown when larger than symbols) are calculated, using simple error propagation, from the standard deviations in Tables 3 and 4. Symbols and regressions are as in Fig. 4.

variables by performing multiple experiments in the same capsule material with the same silicate composition at fixed pressure and temperature. The only variables then are oxygen fugacity and the Si content of the metal. We then

Table 3
Compositions (in wt.%) of co-existing metal and silicate melts from electron microprobe analysis.

Run	Si	Fe	Mo	W	Ni	Co	Total
1.5 GPa metal melts (wt.% element)							
0935	19.42 (0.29)	70.73 (0.35)	0.18 (0.03)	0.16 (0.04)	4.36 (0.05)	4.31 (0.04)	99.15
0936	12.48 (0.08)	77.25 (0.33)	0.15 (0.03)	0.15 (0.04)	4.72 (0.04)	4.00 (0.04)	98.74
BW1007	3.86 (0.05)	88.42 (0.55)	6.76 (0.48)	—	—	—	99.05
BW1008	2.40 (0.03)	90.71 (0.45)	6.74 (0.2)	—	—	—	99.85
BW1009	9.05 (0.13)	85.07 (0.65)	5.55 (0.66)	—	—	—	99.66
BW1015	3.55 (0.02)	91.25 (0.35)	6.05 (0.2)	—	—	—	100.85
BW1027	1.62 (0.02)	85.02 (0.32)	—	—	13.60 (0.08)	—	100.24
BW1029	8.59 (0.09)	83.93 (0.19)	—	—	—	7.27 (0.05)	99.79
BW1030	0.00 (0)	89.48 (0.42)	—	—	11.25 (0.32)	—	100.73
BW1031	0.00 (0)	89.82 (0.24)	—	—	9.69 (0.19)	—	99.51
BW1032	8.75 (0.2)	80.87 (0.32)	—	—	3.93 (0.04)	6.95 (0.1)	100.50
BW1033	8.89 (0.07)	79.85 (0.37)	—	—	4.14 (0.06)	7.32 (0.08)	100.19
BW1034	12.41 (0.25)	74.41 (0.15)	—	—	5.77 (0.04)	7.03 (0.14)	99.62
BW1035	12.49 (0.19)	76.34 (0.43)	—	—	4.37 (0.25)	6.97 (0.17)	100.16
BW1037	12.05 (0.23)	76.77 (0.45)	0.15 (0.04)	—	4.06 (0.03)	6.61 (0.12)	99.64
BW1038	7.53 (0.05)	79.18 (0.29)	0.32 (0.03)	—	4.25 (0.02)	6.81 (0.05)	98.09
BW1039	9.15 (0.15)	70.89 (0.97)	11.11 (1.42)	—	9.06 (0.43)	—	100.21
BW1041	22.14 (0.45)	73.34 (0.36)	—	—	2.10 (0.12)	4.76 (0.09)	102.33
BW1042	22.49 (0.35)	73.23 (0.29)	—	—	2.64 (0.09)	4.02 (0.07)	102.37
BW1043	19.72 (0.18)	70.37 (0.22)	—	—	4.03 (0.09)	4.11 (0.06)	98.23
BW1044	21.61 (0.32)	73.57 (0.31)	—	—	3.24 (0.06)	3.97 (0.05)	102.38
BW1045	11.12 (0.19)	78.32 (0.31)	0.70 (0.11)	—	3.91 (0.3)	3.26 (0.04)	97.31
BW1046	0.80 (0.01)	87.18 (0.27)	0.75 (0.02)	—	6.55 (0.04)	3.70 (0.04)	98.98
BW1047	18.46 (0.37)	67.68 (0.33)	0.55 (0.11)	—	7.45 (0.19)	2.75 (0.05)	96.89
BW1048	7.08 (0.11)	84.07 (0.36)	0.66 (0.17)	—	4.25 (0.03)	2.96 (0.03)	99.02
BW1049	11.96 (0.11)	79.06 (0.36)	0.72 (0.17)	—	2.72 (0.03)	3.29 (0.03)	97.76
BW1050	11.57 (0.1)	79.25 (0.31)	0.66 (0.11)	—	3.57 (0.04)	3.39 (0.03)	98.43
BW1052	11.65 (0.05)	78.17 (0.22)	0.60 (0.04)	—	4.29 (0.04)	3.04 (0.03)	97.75
JT1002	0.00 (0)	91.68 (1.59)	0.23 (0.05)	0.23 (0.02)	6.92 (0.3)	0.10 (0.01)	99.16
JT1008	6.97 (0.04)	87.66 (0.43)	0.23 (0.03)	0.20 (0.03)	3.71 (0.03)	—	98.86
JT1011	6.03 (0.04)	82.48 (0.65)	0.15 (0.01)	0.24 (0.01)	7.47 (0.14)	3.65 (0.02)	100.03
JT1012	1.85 (0.05)	90.94 (0.49)	0.22 (0.02)	0.26 (0.01)	3.69 (0.14)	4.11 (0.05)	101.07
JT1014	0.00 (0)	90.59 (0.44)	0.00 (0.01)	—	9.62 (0.31)	—	100.32
JT1015	3.92 (0.02)	90.01 (0.25)	—	—	6.27 (0.05)	—	100.20
JW1053	14.16 (0.2)	79.73 (0.25)	—	—	3.95 (0.11)	4.06 (0.07)	101.90
JW1054	12.38 (0.09)	78.60 (0.18)	—	—	6.14 (0.04)	4.68 (0.03)	101.80
JW1055	14.29 (0.11)	79.05 (0.24)	—	—	5.05 (0.04)	4.35 (0.04)	102.74
JW1056	12.91 (0.13)	80.06 (0.44)	—	—	5.35 (0.05)	4.24 (0.04)	102.55
6 GPa metal melts (wt.% element)							
C8	0.00 (0)	90.59 (0.58)	0.26 (0.08)	0.25 (0.04)	6.83 (0.04)	0.09 (0.01)	98.02
C11	6.12 (0.16)	83.60 (0.46)	0.18 (0.02)	0.27 (0.01)	6.09 (0.09)	3.96 (0.04)	100.20
C12	11.24 (0.04)	77.99 (0.43)	0.15 (0.03)	0.17 (0.03)	4.92 (0.03)	3.84 (0.01)	98.31
C17	0.92 (0.02)	90.38 (0.65)	0.20 (0.02)	0.25 (0.03)	3.90 (0.08)	3.72 (0.02)	99.38
C18	0.02 (0.01)	87.85 (0.95)	0.22 (0.03)	0.26 (0.01)	8.47 (0.09)	2.33 (0.02)	99.15
C19	0.01 (0)	87.77 (0.27)	0.19 (0.01)	0.19 (0.02)	10.53 (0.04)	2.03 (0.04)	100.73
C20	0.00 (0)	86.54 (0.65)	0.13 (0.09)	0.11 (0.06)	9.07 (0.18)	1.90 (0.04)	97.75
C21	0.01 (0.01)	90.01 (0.79)	0.11 (0.05)	0.13 (0.05)	7.61 (0.16)	1.87 (0.05)	99.74
C22	15.23 (0.34)	71.79 (1.01)	0.19 (0.06)	—	8.87 (0.49)	3.92 (0.1)	100.37
C54	5.78 (0.05)	86.13 (0.27)	—	—	—	8.05 (0.07)	99.97
C56	10.26 (0.52)	76.50 (2.08)	—	—	3.69 (0.12)	6.67 (0.29)	97.12
	SiO_2	FeO	Na_2O	CaO	Al_2O_3	MgO	Total
1.5 GPa silicate melts (wt.% oxide)							
0935	41.05 (0.39)	0.03 (0.06)	0.08 (0.02)	18.31 (2.23)	16.73 (1.31)	24.38 (4.04)	100.59
0936	41.55 (0.43)	0.05 (0.04)	0.10 (0.02)	18.18 (3.43)	17.76 (2.07)	23.43 (6.35)	101.08
BW1007	39.41 (0.38)	0.13 (0.03)	—	15.50 (3.87)	15.41 (4.96)	28.52 (9.19)	98.97
BW1008	40.11 (0.35)	0.22 (0.02)	—	16.62 (5.73)	16.82 (4.77)	27.17 (10.72)	100.94
BW1009	39.24 (0.78)	0.04 (0.02)	—	17.72 (5.86)	15.16 (4.54)	28.58 (10.01)	100.75
BW1015	38.15 (0.56)	0.12 (0.08)	—	19.81 (5.76)	13.85 (3.33)	28.42 (9.01)	100.35
BW1025	39.79 (0.68)	0.08 (0.04)	—	22.75 (6.7)	14.80 (3.96)	24.04 (10.4)	101.47

(*continued on next page*)

Table 3 (*continued*)

	SiO_2	FeO	Na_2O	CaO	Al_2O_3	MgO	Total
BW1026	40.91 (0.36)	0.16 (0.05)	—	21.19 (3.21)	17.43 (2)	22.17 (5.57)	101.86
BW1027	39.03 (0.53)	0.26 (0.02)	—	20.14 (4.47)	15.55 (2.57)	24.97 (7.26)	99.95
BW1028	37.68 (0.68)	0.05 (0.02)	—	19.94 (4.77)	17.07 (3.07)	25.00 (8.16)	99.73
BW1029	39.63 (0.61)	0.12 (0.1)	—	15.95 (4.36)	15.05 (3.11)	28.94 (8.35)	99.69
BW1030	34.27 (1.41)	1.33 (0.23)	—	23.09 (5.87)	12.28 (3.77)	28.77 (8.54)	99.74
BW1031	33.79 (1.41)	3.56 (0.52)	—	22.62 (5.08)	12.59 (3.2)	25.99 (7.78)	98.55
BW1032	39.50 (0.81)	0.04 (0.01)	—	20.55 (7.84)	13.42 (4.68)	26.35 (12.43)	99.86
BW1033	39.91 (0.66)	0.06 (0.02)	0.07 (0.03)	17.14 (6.27)	15.27 (4.81)	28.44 (11.54)	100.89
BW1034	39.62 (0.49)	0.03 (0.01)	—	20.64 (5.38)	13.84 (2.98)	26.08 (8.41)	100.21
BW1035	40.94 (0.49)	0.04 (0.03)	0.08 (0.02)	20.16 (4.48)	16.53 (3.03)	23.26 (7.79)	101.01
BW1037	40.25 (0.46)	0.02 (0.01)	—	19.57 (5.01)	14.32 (2.34)	25.97 (7.71)	100.14
BW1038	38.97 (0.63)	0.06 (0.01)	—	19.65 (4.81)	14.66 (2.64)	26.56 (7.82)	99.89
BW1039	39.99 (0.45)	0.03 (0.01)	—	21.12 (3.97)	14.29 (2.14)	24.05 (6.53)	99.49
BW1041	39.22 (0.52)	0.01 (0.01)	0.06 (0.02)	17.27 (3.61)	14.91 (2.37)	29.01 (6.1)	100.48
BW1042	39.55 (0.47)	0.01 (0.01)	0.07 (0.02)	19.70 (5.61)	14.48 (2.79)	28.35 (8.23)	102.16
BW1043	39.97 (0.49)	0.00 (0)	—	14.28 (4.59)	15.44 (3.92)	31.68 (8.95)	101.38
BW1044	36.24 (2.02)	0.01 (0.01)	0.09 (0.06)	20.79 (8.63)	13.43 (5.44)	31.18 (12.13)	101.73
BW1045	66.09 (0.13)	0.20 (0.04)	—	10.51 (0.04)	11.45 (0.06)	11.83 (0.09)	100.08
BW1046	63.11 (0.08)	3.61 (0.1)	—	6.89 (0.07)	8.64 (0.14)	16.62 (0.25)	98.87
BW1047	65.48 (0.11)	0.04 (0.02)	—	10.22 (0.31)	12.28 (0.23)	11.98 (0.06)	100.00
BW1048	64.93 (0.13)	0.50 (0.04)	—	10.02 (0.09)	12.24 (0.12)	11.80 (0.07)	99.48
BW1049	63.92 (0.45)	0.14 (0.03)	—	10.72 (0.06)	12.42 (0.15)	12.73 (0.2)	99.93
BW1050	60.65 (0.92)	0.16 (0.03)	—	12.00 (0.24)	13.15 (0.49)	12.31 (0.29)	98.27
BW1052	64.28 (0.1)	0.18 (0.05)	—	7.95 (0.07)	9.33 (0.08)	16.87 (0.21)	98.60
JT1002	33.20 (2.9)	5.92 (1.96)	—	15.53 (7.82)	12.39 (5.14)	32.83 (11.76)	99.87
JT1008	37.85 (0.56)	0.08 (0.08)	—	15.86 (4.46)	14.02 (3.19)	31.91 (7.12)	99.73
JT1011	40.30 (7.55)	0.10 (0.07)	0.11 (0.02)	17.15 (2.71)	16.20 (3.48)	25.65 (5.02)	99.51
JT1012	40.43 (0.44)	0.22 (0.01)	0.09 (0.02)	18.40 (2.92)	16.16 (1.5)	24.30 (5.17)	99.59
JT1014	34.87 (1.28)	2.45 (0.26)	—	20.36 (3.45)	11.63 (2.52)	31.93 (4.97)	101.25
JT1015	35.11 (1.08)	0.09 (0.02)	—	20.14 (2.82)	14.01 (2.82)	30.64 (8.25)	99.99
JW1056	37.83 (1.2)	0.02 (0.01)	0.10 (0.05)	22.48 (7.87)	12.61 (3.99)	28.34 (11.01)	101.37
JW1055	34.72 (2.07)	0.01 (0.01)	0.10 (0.05)	21.55 (7.99)	13.58 (4.45)	30.51 (10.78)	100.47
JW1054	39.72 (0.4)	0.07 (0.13)	0.06 (0.01)	16.95 (3.48)	16.87 (2.36)	27.31 (6.04)	101.00
JW1053	38.80 (0.85)	0.02 (0.01)	0.08 (0.03)	20.37 (5.46)	16.83 (4.11)	25.65 (9.2)	101.76
6 GPa silicate melts (wt.% oxide)							
C8	33.38 (1.38)	7.75 (1.98)	—	10.19 (6.05)	12.08 (2.05)	37.51 (7.18)	100.91
C11	38.23 (1.49)	0.18 (0.04)	0.06 (0.06)	12.36 (7.01)	10.10 (4.21)	39.95 (10.27)	100.88
C12	35.92 (1.73)	0.09 (0.12)	—	16.20 (4.79)	12.72 (2.74)	34.65 (5.83)	99.58
C17	35.79 (1.18)	0.59 (0.25)	0.06 (0.03)	13.55 (7.92)	12.43 (1.52)	37.05 (9.45)	99.47
C18	33.75 (1.49)	4.75 (1.18)	0.06 (0.04)	12.70 (5.76)	12.59 (2.14)	35.71 (7.29)	99.57
C19	33.50 (1.83)	10.84 (1.56)	0.06 (0.04)	12.74 (4.39)	10.97 (3.45)	32.39 (5.36)	100.50
C20	31.51 (1.37)	14.02 (2.25)	—	10.86 (4.71)	10.66 (1.86)	32.83 (6.91)	99.88
C21	30.32 (1.18)	20.42 (1.86)	0.04 (0.03)	10.32 (2.72)	10.41 (1.84)	30.15 (4.03)	101.66
C22	37.42 (2.48)	0.05 (0.07)	0.05 (0.05)	8.24 (6.53)	10.02 (6.13)	45.07 (9.47)	100.85
C54	36.36 (1.05)	0.23 (0.51)	—	15.73 (1.46)	11.00 (1.7)	36.21 (1.5)	99.54
C56	37.58 (2.33)	0.10 (0.03)	—	12.19 (6.21)	10.98 (4.75)	39.68 (7.98)	100.52

Numbers in parentheses are 1 standard deviation.

remove oxygen fugacity as a variable by taking account of the fact that the partitioning of Fe between metal and silicate is also oxygen fugacity-dependent.

$$\underset{\text{silicate}}{\text{FeO}} = \underset{\text{metal}}{\text{Fe}} + 0.5\ \text{O}_2$$

We eliminate oxygen by combining Reactions (2) with the Fe-reaction (above) as follows:

$$\underset{\text{silicate}}{\text{MO}_{n/2}} + \frac{n}{2}\underset{\text{metal}}{\text{Fe}} = \underset{\text{metal}}{\text{M}} + \frac{n}{2}\underset{\text{silicate}}{\text{FeO}} \quad (3)$$

The equilibrium constant for equilibrium (3) is independent of oxygen fugacity and may be defined as follows in terms of mole fractions X_i and activity coefficients γ_i in metal and silicate phases:

$$K = \frac{X_{\text{M}}^{\text{met}}\gamma_{\text{M}}^{met}\left(X_{\text{FeO}}^{\text{sil}}\gamma_{\text{FeO}}^{\text{sil}}\right)^{n/2}}{X_{\text{MO}_{n/2}}^{\text{sil}}\gamma_{\text{MO}_{n/2}}^{\text{sil}}\left(X_{\text{Fe}}^{\text{met}}\gamma_{\text{Fe}}^{\text{met}}\right)^{n/2}} \quad (4)$$

Since the silicate compositions are fixed with respect to major elements, activity coefficients γ_i are constant and, taking

Table 4
Trace-element contents (in ppm) from LA-ICP–MS analyses of experimental runs.

Run	V	Cr	Co	Ni	Nb	Mo	W
1.5 GPa metal melts							
0935	1540 (43)[a]	1690 (55)	—[b]	—	1520 (52)	1900 (30)	1960 (53)
0936	—	—	—	—	—	1650 (79)	2160 (110)
BW1032	—	—	—	36,700 (218)	—	—	—
BW1037	—	—	—	36,000 (80)	—	—	—
BW1038	—	—	—	39,700 (57)	—	—	—
BW1039	—	—	—	79,300 (57)	—	—	—
BW1045	3000 (35)	3250 (39)	28,200 (38)	33,100 (357)	—	5700 (100)	7500 (200)
BW1046	742 (9)	785 (4)	29,200 (372)	51,600 (865)	—	—	—
BW1047	2670 (19)	—	23,300 (133)	60,800 (374)	—	4800 (40)	5500 (50)
BW1048	2540 (47)	2380 (17)	25,000 (227)	34,700 (447)	—	5800 (100)	7800 (200)
BW1049	3200 (70)	3340 (17)	27,700 (180)	23,000 (226)	—	5900 (200)	8000 (500)
BW1050	3030 (51)	3110 (52)	28,600 (114)	29,500 (449)	—	5900 (100)	7500 (300)
BW1052	2850 (140)	2680 (24)	24,900 (307)	34,500 (529)	—	5000 (300)	6700 (400)
JT1002	113 (40)	349 (29)	—	65,000 (1050)	9 (3)	2820 (346)	3200 (197)
JT1008	2010 (55)	1760 (47)	—	32,400 (647)	2290 (66)	—	—
JT1011	1570 (21)	1460 (95)	—	—	1840 (179)	—	2200 (39)
JT1012	1890 (35)	1790 (69)	—	—	2270 (230)	—	3040 (110)
JT1014	—	—	—	84,300 (1220)	—	—	10 (1)
JT1015	—	—	—	55,700 (762)	—	—	—

	Cr	Co	Ni	Nb	Mo	W
6 GPa metal melts						
C8	792 (210)	83 (10)	66,400 (863)	21 (4)	2800 (163)	3560 (136)
C11	1710 (52)	35,700 (263)	59,300 (710)	1990 (57)	—	—
C12	1440 (29)	36,000 (207)	47,300 (636)	1580 (93)	1790 (81)	1990 (81)
C17	1700 (63)	35,800 (180)	39,300 (308)	1790 (190)	—	3020 (51)
C18	621 (67)	22,100 (198)	84,300 (287)	37 (22)	2720 (89)	3190 (50)
C19	189 (55)	20,200 (282)	112,000 (1370)	—	1990 (118)	2770 (348)
C20	107 (32)	18,700 (50)	91,400 (517)	—	2080 (179)	2130 (86)
C21	—	18,600 (127)	81,100 (1020)	—	1740 (31)	1430 (30)
C22	1590 (32)	36,400 (501)	87,100 (1820)	1600 (57)	1970 (90)	2100 (84)
C54	—	69,300 (219)	—	—	—	—
C56	—	63,000 (386)	34,600 (171)	—	—	—

	V	Cr	Co	Ni	Nb	Mo	W
1.5 GPa silicate melts							
0935	3 (1)	5 (3)	—	—	0.60 (22)	0.20 (10)	1.65 (38)
0936	—	—	—	—	—	4.06 (196)	8.04 (210)
BW1007	—	—	—	—	—	3.97 (69)	—
BW1008	—	—	—	—	—	0.68 (34)	—
BW1009	—	—	—	—	—	0.82 (59)	—
BW1015	—	—	—	—	—	0.13 (5)	—
BW1027	—	—	—	3.93 (63)	—	—	—
BW1030	—	—	—	9.8 (11)	—	—	—
BW1031	—	—	—	13 (1)	—	—	—
BW1032	—	—	—	0.93 (17)	—	—	—
BW1033	—	—	—	2.48 (81)	—	—	—
BW1034	—	—	—	0.63 (10)	—	—	—
BW1035	—	—	—	0.78 (23)	—	—	—
BW1037	—	—	—	0.51 (37)	—	—	—
BW1038	—	—	—	0.95 (39)	—	—	—
BW1039	—	—	—	1.25 (50)	—	—	—
BW1041	—	—	—	0.23 (8)	—	—	—
BW1042	—	—	—	0.25 (6)	—	—	—
BW1043	—	—	—	1.47 (23)	—	—	—
BW1044	—	—	—	0.26 (13)	—	—	—
BW1045	202 (4)	280 (30)	6.34 (50)	4.15 (43)	—	0.38 (20)	3.65 (130)
BW1046	1450 (40)	1400 (90)	39.2 (8)	9.76 (85)	—	—	—
BW1047	23 (1)	—	1.79 (30)	1.85 (53)	—	0.12 (9)	4.23 (10)

(*continued on next page*)

Table 4 (*continued*)

	V	Cr	Co	Ni	Nb	Mo	W
BW1048	434 (15)	610 (50)	8.51 (90)	5.05 (160)	—	0.20 (10)	4.31 (206)
BW1049	130 (5)	250 (20)	5.34 (50)	1.88 (20)	—	0.39 (6)	13.80 (320)
BW1050	181 (14)	290 (8)	5.59 (120)	3.46 (120)	—	0.18 (7)	15.20 (1100)
BW1052	158 (4)	290 (20)	7.65 (140)	6.65 (130)	—	0.38 (19)	5.77 (110)
JT1002	704 (70)	470 (47)	—	26 (6)	1990 (228)	1.35 (13)	43.3 (33)
JT1008	29 (2)	39 (5)	—	1.41 (70)	13.1 (6)	—	—
JT1011	40 (3)	53 (6)	—	—	17.4 (8)	—	1.40 (52)
JT1012	175 (5)	170 (2)	—	—	251 (8)	—	1.23 (93)
JT1014	—	—	—	13.5 (6)	—	—	0.06 (4)
JT1015	—	—	—	1.16 (60)	—	—	—
JW1053	—	—	—	0.53 (21)	—	—	—
JW1054	—	—	—	4.30 (15)	—	—	—
JW1055	—	—	—	0.45 (7)	—	—	—
JW1056	—	—	—	0.32 (8)	—	—	—

	Cr	Co	Ni	Nb	Mo	W
6 GPa silicate melts						
C8	810 (40)	0.43 (8)	72 (6)	1710 (181)	2.76 (44)	78 (10)
C11	60 (8)	7.46 (208)	3.69 (160)	54 (1)	—	—
C12	16 (3)	33 (4)	9.7 (7)	5.97 (10)	1.59 (46)	1.23 (24)
C17	140 (8)	11 (1)	5.4 (5)	428 (23)	—	1.12 (63)
C18	520 (50)	63 (2)	55 (1)	1370 (74)	0.84 (13)	13.5 (130)
C19	370 (30)	116 (10)	99 (6)	—	3.91 (130)	548 (220)
C20	480 (20)	181 (9)	168 (6)	—	4.29 (66)	204 (20)
C21	—	203 (14)	156 (30)	—	6.31 (56)	321 (51)
C22	11 (5)	18 (2)	21 (1)	0.94 (18)	2.81 (50)	7.19 (160)
C54	—	18 (3)	—	—	—	—
C56	—	3.6 (8)	6.16 (180)	—	—	—

Runs BW1007, BW1008, BW1009, BW1015, BW1025, BW1026, BW1027, BW1028, BW1029, BW1030, BW1031, BW1033, BW1034, BW1035, BW1041, BW1042, BW1043, BW1044, JW1053, JW1054, JW1055 and JW1056 used the electron microprobe analysis of the metal melts for Ni, Mo and W.

[a] Numbers in parentheses are 1 standard deviation expressed in terms of least digits.

[b] Not determined.

account of the difference in atomic weights, K is related to the weight partition coefficient ratio K_D:

$$K = a \cdot \frac{[\mathrm{M} \cdot \gamma_\mathrm{M}]_\mathrm{met}[\mathrm{FeO}]^{n/2}_\mathrm{sil}}{[\mathrm{MO}_{n/2}]_\mathrm{sil}[\mathrm{Fe} \cdot \gamma_\mathrm{Fe}]^{n/2}_\mathrm{met}} = b \cdot K_D \cdot \frac{\gamma^\mathrm{met}_\mathrm{M}}{\gamma^{\mathrm{met}^{n/2}}_\mathrm{Fe}} = \frac{b \cdot D_\mathrm{M}}{D^{n/2}_\mathrm{Fe}} \frac{\gamma^\mathrm{met}_M}{\gamma^{met^{n/2}}_\mathrm{Fe}} \quad (5)$$

In Eq. (5), a and b are constants containing, respectively, the ratio of activity coefficients in the silicate and the conversions from mole fractions to weight fractions. If the ratio of activity coefficients in the metal is constant then K_D should also be constant and should not be affected by changing Si content of the metal. Conversely, dependence of K_D on Si indicates that there are non-ideal M–Si and/or Fe–Si interactions in the metallic liquid.

Formulating K_D requires knowledge of the oxidation state of the trace metal M in the silicate liquid. Under reducing conditions (below the IW buffer) Fe, Ni, Cr and Co should all be in the 2+ oxidation state (Kegler et al., 2008; Wood et al., 2008), V 3+ oxidation state (Wood et al., 2008) and Nb 5+ (Wade and Wood, 2001). Although Mo and W can exhibit both 4+ and 6+ oxidation states in the oxygen fugacity range below the IW buffer (O'Neill and Eggins, 2002; O'Neill et al., 2008), Mo should be dominantly 4+ under the conditions where the metal contains significant Si (O'Neill et al., 2008). Based on the FeO/Fe ratios of our Si-bearing experiments, oxygen fugacity was in the range of 2.5–7 log units below the IW buffer, which brings us into the realm of mixed 4+ and 6+ oxidation states for W (O'Neill et al., 2008). Thermodynamic data for oxides (Barin et al., 1989) indicate that the 4+ oxidation state should dominate below IW at 1900–2100 K however. A preliminary study performed in our laboratory of $D_\mathrm{W}/D_\mathrm{Mo}$ at 1.5 GPa and >1900 K also indicates that Mo and W have essentially the same oxidation state if fO_2 is less than ~2.8 log units below IW. We have therefore assumed that W is dominantly in the 4+ oxidation state.

Figs. 4 and 5 are plots of K_D versus the Si content of the metal. As can be seen, Cr and Nb partitioning depends little on Si, while Ni, Co, Mo and W are strongly controlled by the Si concentration in the metal. V partitioning is less strongly controlled by the Si content of the metal. The offset in trends of K_D for W, V and Mo between MgO and SiO_2 capsule experiments reflects differences in activity coefficient of the trace element in the silicate melt in these different

capsules (MgO saturated vs. SiO_2 saturated). In effect, the trace element oxide is less soluble in SiO_2-rich melts than in MgO-rich melts. In order to model the effects of metal composition we used the epsilon-model (ε-model; Wagner, 1962) of non-ideal interactions in Fe liquids. When modified to ensure consistency with the Gibbs–Duhem equation (Ma, 2001) this leads to the following expression for the activity coefficients of Fe and trace metal M in a ternary alloy in the system Fe–Si–M:

$$\ln\gamma_{Fe} = \varepsilon_{Si}^{Si}(x_{Si} + \ln(1-x_{Si})) + \varepsilon_{M}^{M}(x_M + \ln(1-x_M)) + \varepsilon_{M}^{Si}x_{Si}x_M\left(1 - \frac{1}{1-x_M} - \frac{1}{1-x_{Si}}\right) - \frac{\varepsilon_{M}^{Si}}{2}x_{Si}^2x_M^2\left(\frac{3}{1-x_M} + \frac{3}{1-x_{Si}} + \frac{x_{Si}}{(1-x_{Si})^2} + \frac{x_M}{(1-x_M)^2} - 3\right) \quad (6)$$

$$\ln\gamma_M = \ln\gamma_{Fe} + \ln\gamma_M^O - \varepsilon_M^M\ln(1-x_M) - \varepsilon_M^{Si}x_{Si}\left(1 + \frac{\ln(1-x_{Si})}{x_{Si}} - \frac{1}{1-x_M}\right) + \varepsilon_M^{Si}x_{Si}^2x_M\left(\frac{1}{1-x_M} + \frac{1}{1-x_{Si}} + \frac{x_M}{2(1-x_M)^2} - 1\right) \quad (7)$$

In Eqs. (6) and (7) x_i refers to the mole fraction of i in the metal γ_i is the activity coefficient of i, γ_i^O is the activity coefficient of i infinitely dilute in liquid Fe and ε_i^j is the interaction parameter between elements i and j. Deviations from Henry's Law are accounted for by the ε_M^M terms. The principal reason for using this approach is that many interaction parameters have been experimentally measured and are presented in the form of ε_i^n values (Steelmaking, 1988), which means that our experimental data can be built directly onto a large existing database. In the discussion that follows, ε_i^j values have been extrapolated from the experimental temperature to 1873 K using the relationship from the Steelmaking Data Sourcebook:

$$\varepsilon_i^j(T) = \frac{1873}{T}\varepsilon_i^j\ (1873)$$

Use of this relationship ensures that all interactions approach zero at infinite temperature. Note, however, that our extrapolation is over only 50° for the 1.5 GPa experiments and 250° for the 6 GPa data.

3.1. Nickel

As can be seen from Fig. 4, the partitioning of Ni between metal and silicate is strongly dependent on the Si content of the metal. Using the epsilon-model with tabulated values of ε_{Si}^{Si} of either 12.4 (Steelmaking, 1988) or 8.6, which is more consistent with the study of Bouchard and Bale (Bouchard and Bale, 1995) leads to ε_{Si}^{Ni} of approximately 7 at both 1.5 and 6 GPa. This non-ideality is much larger than anticipated from the ε_{Si}^{Ni} value of 1.2 estimated from the effect of Ni on Si solubility in liquid Fe (Chipman, 1955), but the consistency between our two sets of data makes it difficult to argue for a value substantially different from 7. Linear regression of all the 1.5 GPa data leads to ε_{Si}^{Ni} of 7.5(0.8) where the value in brackets is 1 standard error. The value of 7.5 applies at 1873 K as discussed above.

3.2. Cobalt

There are relatively few data in the literature bearing on the effect of Si on Co activity in liquid Fe and for this reason we are unable to compare our results with earlier data. As with Ni, however, the effect of Si on partition coefficients is considerable (Fig. 4) Linear regression of the 1.5 GPa data from experiments performed in SiO_2 capsules leads to a value of ε_{Si}^{Co} of 4.6(0.7). This value is also consistent with the 6 GPa data, albeit from experiments in MgO capsules (Fig. 4).

3.3. Molybdenum

Molybdenum is well-known to interact strongly with Si in liquid Fe and the value of ε_{Si}^{Mo} tabulated in the Steelmaking Data Sourcebook is 933. A more recent experimental study (Ono-Nakazato et al., 2007) gives a much lower value of 43 ± 13 at Si concentrations up to 3.06% Si. Our experimental results were obtained over a much wider range of Si content of the metal, 0–19.4% and yield (Fig. 5) a slightly smaller epsilon value than that obtained by Ono-Nakazato et al. (2007). Because, as can be seen from Fig. 5, Mo partitioning depends on the composition of the silicate liquid, we are unable to aggregate our experiments in MgO and SiO_2 capsules into s single data set. Therefore, we obtained epsilon from the data covering the widest range of Si contents, which is for MgO capsule experiments at 1.5 GPa. Linear regression yields ε_{Si}^{Mo} of 22(5). This value is, as can be seen from Fig. 5, consistent with data obtained in SiO_2 capsules and with the 6 GPa results.

3.4. Tungsten

Fig. 4 indicates that there are strong Si–W interactions in liquid Fe and there is consistency between 1.5 and 6 GPa data and results in MgO and SiO_2 capsules. Linear regression of the largest data set, in MgO capsules at 1.5 GPa yields ε_{Si}^{W} of 18.3(2.8). We are unaware of any literature data with which this result can be compared.

3.5. Vanadium

As can be seen from Fig. 5, the influence of Si on metal–silicate partitioning of V is weaker than the elements described above, leading to ε_{Si}^{V} of about 2. This is compared on the figures with the slightly higher value of 5.36 from the Steelmaking Data Sourcebook.

3.6. Chromium and niobium

The metal–silicate partitioning of Cr and Nb is only weakly dependent on the Si content of the metal (Fig. 5) and, as can be seen from the lines plotted on the figures, our results broadly agree with the values of ε_{Si}^{Cr} (0.03) and ε_{Si}^{Nb} (0.29) in the Steelmaking Data Sourcebook.

4. DISCUSSION

It has been known for some time (Thibault and Walter, 1995; Li and Agee, 2001) that partitioning of Ni and Co between metal and silicate is strongly dependent on pressure and that the observed Ni and Co contents of the silicate Earth imply pressures of metal–silicate equilibrium of greater than 25 GPa. When metal–silicate partitioning for other refractory elements, notably weakly siderophile V, Cr and Nb are considered in conjunction with partitioning for Ni, Co and W (Wade and Wood, 2005; Wood et al., 2008), much better constraints on core formation emerge. In order to satisfy the estimated core–mantle partitioning of V, Ni and Co given in Table 1, pressures of core formation would be on the order of 42 GPa with temperatures about 4500 K, 1300° above the liquidus temperature of the mantle. The result, would be a core containing about 30% Si and >60% of the Earth's niobium, figures about 4 times the plausible amounts (Allègre et al., 1995; Table 1). In order to more closely match the estimated core–mantle partitioning, Wade and Wood (2005) constructed a model consistent with the physical concept of a deep magma ocean. In this model, accreting material is added to the upper mantle and the added metal is equilibrated with the mantle before accumulating in a layer at intermediate depth. The latter corresponds to the depth of the magma ocean and the point at which the underlying mantle becomes solid. Gravitational instabilities of the metal layer lead to periodic generation of large diapirs (Stevenson, 1981), which sink rapidly to the core without further equilibration. The implication is that the final metal–silicate equilibration temperature is close to the liquidus of the mantle silicate at some intermediate depth. In this case it is possible to grow the Earth with temperatures fixed on the silicate liquidus and match the Ni, Co, W, V, Cr and Nb contents of the silicate Earth. From Ni and Co partitioning, the magma ocean is calculated to maintain a thickness approximately 35% of the depth to the core–mantle boundary in the growing Earth. In order to satisfy the V, Cr and Nb contents of the mantle, however, it is necessary that much of the Earth accreted under conditions much more reducing than those corresponding to the current oxidised mantle Fe content of 6.26%. If there is no change in oxidation state, V appears not to be siderophile enough. At low pressures and oxygen fugacities corresponding to the current Fe content of the mantle, Cr, V, Si and Nb are essentially lithophile while Ni, Co and W are strongly siderophile (Mo is excluded from consideration because of inadequate partitioning data). As oxygen fugacity is reduced, Cr, V and Nb eventually become somewhat siderophile, Si remains lithophile and Ni, Co and W remain strongly siderophile. Increasing pressure and temperature as the planet grows leads to increasingly siderophile character of Cr, V, Nb and Si while Ni, Co and W become less siderophile. Matching of the overall partition coefficients with the values of Table 1 therefore requires a balance between pressure/temperature conditions, which increase with increasing planet size and the oxygen fugacity of core segregation. In practice Wood et al. (2008) found that V, Cr and Nb core–mantle partitioning is reproduced if the oxidised Fe content of the mantle increased from ~1% to the current value of 6.26% as the Earth grew. Their model also reproduces the calculated core–mantle partitioning of Ni, Co and W and yields a Si content of the core of approximately 7%, in good agreement with cosmochemical estimates (Allègre et al., 1995).

In the context of the current study, increasing oxidation state of the Earth during accretion is consistent with a significant Si content of the segregating core. The latter must, as we have shown here, feedback into the partitioning of, in particular, Ni, Co and W, the principal elements that constrain the pressure of equilibration. Since these elements all become less siderophile with increasing Si content of the metal (Figs. 4 and 5) the net effect should be to lower the pressure of equilibration given by their core–mantle partitioning. In addition, it has recently been shown that oxygen is to some extent soluble in liquid Fe at high pressures and temperatures (Asahara et al., 2007; Ozawa et al., 2008). This element is known to interact strongly with V and Nb in the metal, making them much more siderophile (Corgne et al., 2009) so that the dissolution of oxygen should not be ignored when constructing core segregation scenarios.

In order to test the influence of Si and O as light elements on partitioning into the core it is necessary to develop an internally consistent model in which pressure, temperature and oxygen fugacity (expressed as $D_{Fe} = \frac{[Fe]_{metal}}{[Fe]_{silicate}}$ where Fe in the silicate is oxidised) are factored into the partitioning of the light elements as well as the siderophile elements of interest. We used our new results together with those in the literature to fit partitioning of Si (4+ oxidation state) as a function of pressure, temperature and the composition of the silicate melt. Partitioning of Si and Fe between metal and silicate can be expressed in terms of the exchange reaction:

$$\underset{\text{silicate}}{SiO_2} + 2\underset{\text{metal}}{Fe} = \underset{\text{metal}}{Si} + 2\underset{\text{silicate}}{FeO} \tag{8}$$

Using the general temperature and pressure-dependence of the equilibrium constant and adding activity coefficients for the silicate back into Eq. (5) we have:

$$\log K' + \log\left[\frac{\gamma_{Si}^{met}}{\gamma_{Fe}^{met\,2}}\right] = A + \frac{B}{T} + \frac{cP}{T} + e\log\left[\frac{\gamma_{SiO_2}^{sil}}{\gamma_{FeO}^{sil\,2}}\right] \tag{9}$$

K' is given by the experimentally determined compositions of metal and silicate phases, in terms of mole fractions X_i as follows:

$$K' = \frac{X_{Si}^{met}\left(X_{FeO}^{sil}\right)^2}{X_{SiO_2}^{sil}\left(X_{Fe}^{met}\right)^2}$$

In practice K' can readily be recalculated to the ratio of weight partition coefficients ($\frac{D_{Si}}{D_{Fe}^2}$). The activity coefficients in the metal were calculated at the temperature of the experiment from the epsilon-model using the ε and γ_i^O values of Table 5. The conventional approach to estimating the silicate activity coefficient on the right hand side is to parameterise it as a function of the ratio of non-bridging oxygen atoms to tetrahedral cations, (NBO/t). However, the link between a structural descriptor, such as NBO/t, and chemical activity in the melt is tenuous at best (O'Neill

Table 5
Interaction parameters and infinitely dilute solute activity coefficients used in our calculations.

	Si	Ni	Co	W	Mo	Cr	V	Nb
γ^{O}	0.0045 (0.0013)[a]	0.66	0.55	1	1	1	0.08	0.2
ε^{Si}	8.6 (12.4)	7.5 (1.2)	4.6 (−)	18.3 (−)	22 (933)	0.03	2.0 (5.4)	0
ε^{O}	−7.1	1.4	1.9	4.1	1.3	−9.9	−2.9	−47
ε^{M}	8.6	0.12	1.18	0	4.1	−0.1	6.6	0

[a] All data from the Steelmaking Data Sourcebook at 1873 K except where an updated version is given in the text. In the latter case, values from the Steelmaking data Sourcebook are given in parentheses. ε^{Si}, ε^{o} and ε^{M} refer, respectively, to interaction parameters with Si, O and the element itself.

Table 6
Partitioning equations used to model accretion as shown in Fig. 7.

$\log D_{Ni}\gamma_{Ni} = \log D_{Fe}\gamma_{Fe} + 0.67 + 3097/T - 114P/T$[a]
$\log D_{Co}\gamma_{Co} = \log D_{Fe}\gamma_{Fe} - 0.05 + 2511/T - 56P/T$[a]
$\log D_{W}\gamma_{W} = 2.2\log D_{Fe}\gamma_{Fe} - 0.1 + 1128/T - 112P/T$[b]
$\log D_{Cr}\gamma_{Cr} = \log D_{Fe}\gamma_{Fe} + 0.78 - 4522/T - 23P/T$[c]
$\log D_{V}\gamma_{V} = 1.5\log D_{Fe}\gamma_{Fe} + 0.55 - 8548/T - 46P/T$[c]
$\log D_{Nb}\gamma_{Nb} = 2.5\log D_{Fe}\gamma_{Fe} + 1.46 - 13{,}240/T - 199P/T$[c]
$\log D_{Si}\gamma_{Si} = 2\log D_{Fe}\gamma_{Fe} + 0 - 14{,}338/T$[d]

T, temperature (K); P, pressure (GPa). Note that the values derived by the authors concerned have been adjusted within quoted uncertainties to create Fig. 7.
[a] Wade and Wood (2005).
[b] Cottrell et al. (2009).
[c] Wood et al. (2008).
[d] This study — for pyrolite only.

and Eggins, 2002; O'Neill et al., 2008). Because of this we follow O'Neill and Eggins and use a regular solution model of the major oxide components to evaluate the silicate activity coefficient.

Multiplying Eq. (9) by R (gas constant) and temperature and parameterising the silicate activity coefficient term on the right hand side in terms of a regular solution leads to:

$$RT\left(\log K' + \log\left[\frac{\gamma_{Si}^{met}}{\gamma_{Fe}^{met^2}}\right]\right) = A + bT + cP + \left(e_0 + e_{12}X_1^{sil}X_2^{sil} + \cdots + e_{jk}X_j^{sil}X_k^{sil}\right) \quad (10)$$

We performed stepwise linear regression (using the SPSS package) of the left hand side of Eq. (10) against P, T and the silicate compositional terms for the 61 experiments shown in Fig. 6. In each case K_D was calculated from the reported compositions of metal and silicate phases while activity coefficients for the metal were calculated from the epsilon-model with the interaction parameters of Table 5. The result, shown in Fig. 6 is that neither the pressure nor the temperature terms are statistically significant (from the F-test) leading to:

$$\log K' + \log\left[\frac{\gamma_{Si}^{met}}{\gamma_{Fe}^{met^2}}\right] = \frac{e_0 + e_1X_{CaO}^{sil}X_{MgO}^{sil} + e_2X_{MgO}^{sil\ 2} + e_3X_{CaO}^{sil}X_{SiO_2}^{sil}}{RT} \quad (11)$$

We found that the only statistically significant melt compositional terms are those shown in Eq. (11) and our fitted equation yielded e_0 of −77,970 (4585), e_1 of -1.824×10^5 (34,910), e_2 of -1.334×10^5 (136,06) and e_3 of

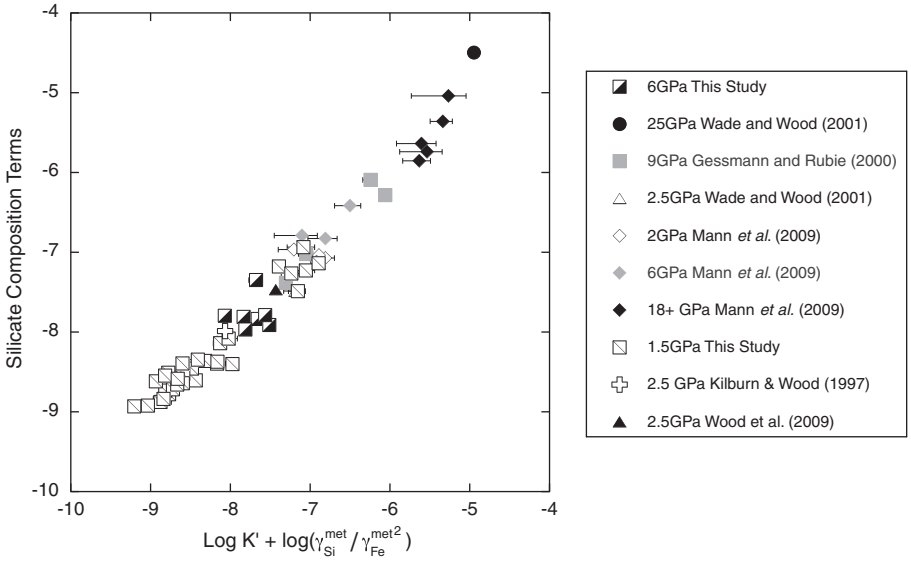

Fig. 6. Plot of $\log K' + \log(\gamma_{Si}^{met}/\gamma_{Fe}^{met^2})$, corrected for metal composition, versus silicate composition terms from Eq. (11). The variation in partitioning can be explained solely by changes in metallic and silicate melt composition and additional terms in pressure and temperature are not (from the F-test) statistically significant.

-4.202×10^5 (66,318). As an alternative fitting approach we used the Wade and Wood (2005) method and constrained the temperature effect on K_D using the 1-atmosphere thermodynamic data of Barin et al. (1989). Fitting in the same way then produced a pressure term in addition to the compositional terms discussed above because temperature and pressure are strongly correlated in the experimental dataset. In terms of calculated Si content of the core from our modelling (Section 5) the two results are very similar and we have therefore used the simpler equation (above) for our modelling. Note that for pyrolite composition the expression above simplifies to:

$$\log K' + \log\left[\frac{\gamma_{Si}^{met}}{\gamma_{Fe}^{met\,2}}\right] = \frac{-14,338}{T}$$

5. A CONTINUOUS ACCRETION MODEL TAKING ACCOUNT OF SI AND O AS LIGHT ELEMENTS

In order to determine the impact of our measured interaction parameters on the continuous growth and oxidation model we used the Si partition coefficient equation derived by least squares fitting (Eq. (11)) and added the oxygen solubility model of Ozawa et al. (2008). Since the latter is based on FeO partitioning between magnesiowüstite and metal, we corrected for the fact that FeO is dissolved in silicate melt in our model using the magnesiowüstite–melt partition coefficients of Asahara et al. (2007). We then grew the Earth in 1% increments, keeping the temperature of equilibration on the silicate liquidus (Zhang and Herzberg, 1994; Zerr et al., 1998; Tronnes and Frost, 2002; summarised by Wood et al., 2008) and allowing pressure to increase as a fixed fraction of the increasing pressure at the core–mantle boundary. At each step we took explicit account of the effects of Si and O on metal–silicate partitioning of each of the elements of concern. To do this we used our new Si–metal interaction parameters together with O–metal interaction parameters from the literature (Table 5). Partitioning of the pressure-sensitive elements Ni, Co and W constrains the pressure to be maintained at ~28% of the pressure at the core–mantle boundary which leads to a maximum pressure of ~36 GPa as shown in Fig. 7. Note that pressures are 5 GPa lower than in our previous work (Wood et al., 2008) because dissolution of Si into the metal diminishes the siderophile character of Ni, Co and W. The overall result is relatively insensitive to the oxygen fugacity path taken during accretion because, as shown in Fig. 7, Ni, Co and W are only significantly retained in the mantle during the latest high pressure, high fO_2 stages of core segregation. As in our previous work, however (Wade and Wood, 2005), we found that the only way to match the concentrations of V, Cr and Nb in the silicate Earth with the partition coefficients of Table 1 was to allow the Earth to oxidise as accretion progressed, as shown in Fig. 7. The lower pressures and temperatures consistent with partitioning of Ni, Co and W between core and mantle in the presence of Si mean that the constraints on reducing conditions during accretion to explain V and Cr partitioning are even more stringent than in our earlier work, as shown in Fig. 7. We assume that the last 10% of partitioning was at the current

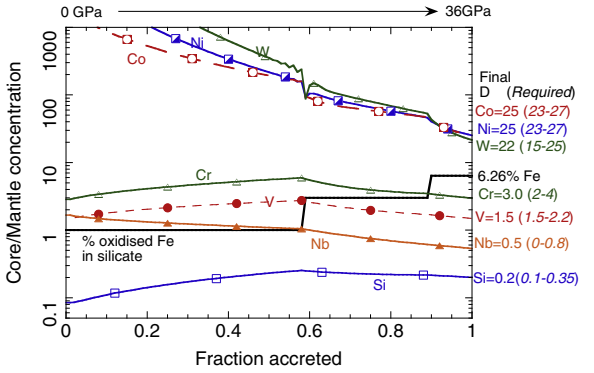

Fig. 7. Continuous accretion model, which reproduces the estimated core–mantle partitioning behaviour of Table 1. Note that oxygen fugacity, as represented by the oxidised Fe content of the mantle must, during most of accretion, be substantially lower than implied by the current oxidised Fe content of the mantle. Interactions of siderophile elements with Si and O were explicitly considered during accretion and the resulting model implies ~4.3 wt.% Si and 0.15% O in the core. Metal–silicate partitioning data, adjusted within uncertainty to improve fit, were taken from Wade and Wood (2005) for Ni, Co, Wood et al. (2008) for V, Cr, Nb and Cottrell et al. (2009) for W (see Table 6).

oxidised Fe content of the mantle (6.26%) and allowed the mantle to oxidise in 2 steps from 1.0% Fe to this value. The resultant Si and O contents of the mantle are 4.3 wt.% and 0.15%, respectively. Taking account of 1 standard error uncertainties in Si partitioning (Eq. (11)), leads to an associated uncertainty of ±1.2% in Si concentration in the metal. The value of 4.3(1.2) wt.% Si in the core is in excellent agreement with an estimate based on experimental measurements of Si isotope partitioning between metal and silicate (Shahar et al., 2009). These authors concluded that the observed $\delta^{30}Si$ of silicate Earth implies that the core contains 2–6 wt.% Si. Our calculation is also broadly consistent with estimates based on sound velocity measurements for Si-bearing alloys at extreme pressure (e.g., Badro et al., 2007). It should be noted that if we add 2–3% S to the metal then, using published interaction parameters (Steelmaking, 1988) the calculated effect on Fig. 7 is negligible.

6. CONCLUSIONS

Data in the Steelmaking Data Sourcebook show that metal–silicate partitioning of many elements should be sensitive to the composition of the Fe-rich liquid alloy, notably its contents of Si, C and O. Since Si now appears likely to be a significant component of the "light" elements dissolved in Earth's core (Georg et al., 2007; Fitoussi et al., 2009) we determined the effects of Si on liquid metal–liquid silicate partitioning of Ni, Co, Mo, W, V, Cr and Nb at 1.5 GPa/1923 K and 6 GPa/2123 K under conditions of constant silicate melt composition.

As Si is added to liquid Fe metal under conditions of fixed oxygen fugacity, Ni, Co, W, Mo and V all become progressively less siderophile. In terms of the ε-model (Wagner, 1962) ε_{Si}^{Ni} is found to be 7.5 at 1873 K. Corresponding values for interaction of Si with Co, W and Mo are 4.6, 18.3 and 22, respectively. The weakly siderophile

elements V, Cr and Nb interact less strongly (in the case of V) or only weakly with Si in liquid Fe.

Experimental Si partitioning data have been used to obtain a relationship between the metal–silicate distribution of Si and temperature and silicate melt composition (expressed in terms of a regular solution model). Within the uncertainties in the partitioning data we are able to ignore terms in pressure and temperature, leading to the following expression:

$$\log K' + \log\left[\frac{\gamma_{Si}^{met}}{\gamma_{Fe}^{met\,2}}\right] = \frac{e_0 + e_1 X_{CaO}^{sil} X_{MgO}^{sil} + e_2 X_{MgO}^{sil\,2} + e_3 X_{CaO}^{sil} X_{SiO_2}^{sil}}{RT}$$

When applied to pyrolite composition the fit parameters yield the following equation:

$$\log K' + \log\left[\frac{\gamma_{Si}^{met}}{\gamma_{Fe}^{met\,2}}\right] = \frac{-14,338}{T}$$

K' is the ratio of compositions in metal and silicate phases expressed as mole fractions X:

$$K' = \frac{X_{Si}^{met}\left(X_{FeO}^{sil}\right)^2}{X_{SiO_2}^{sil}\left(X_{Fe}^{met}\right)^2}$$

We used our data on Si interactions and partitioning in conjunction with published metal–silicate partitioning results for siderophile elements to develop a model of continuous accretion and core segregation. In this case we took explicit account of the partitioning of Si (this study) and O (from Ozawa et al., 2008) between metal and silicate and their effects on metal–silicate partitioning of siderophile elements. We find that the effect of Si on the siderophile characteristics of Ni, Co and W means that the pressures of core segregation estimated from these elements are ~5 GPa lower than those derived from experiments in which the metal contained negligible Si (e.g., Wade and Wood, 2005). The core–mantle partitioning of V, Cr and Nb requires that most of Earth accretion took place under conditions which were much more reducing than those implied by the current FeO content of the mantle and that the oxidation took place late in the accretionary process. Paths of terrestrial accretion, oxidation state and partitioning which are consistent with the current mantle contents of Ni, Co, W, V, Cr and Nb lead to Si and O contents of the core of ~4.3 wt.% and 0.15%, respectively.

ACKNOWLEDGMENTS

This work was supported by Natural Environmental Research Council (UK) grant NE/F018266/1 to B.J.W. We thank Norman Charnley for much assistance in electron microprobe analysis and Sally Gibson and Jason Day for the use, technical advice and assistance of the laser ablation ICP–MS facility at the University of Cambridge.

REFERENCES

Allègre C. J., Poirier J.-P., Humler E. and Hofmann A. W. (1995) The chemical composition of the Earth. *Earth Planet. Sci. Lett.* **134**, 515–526.

Asahara Y., Frost D. J. and Rubie D. C. (2007) Partitioning of FeO between magnesiowüstite and liquid iron at high pressures and temperatures: implications for the composition of Earth's outer core. *Earth Planet. Sci. Lett.* **257**, 435–449.

Badro J., Fiquet G., Guyot F., Gregoryanz E., Occelli F., Antonangeli D. and d'Astuto M. (2007) Effect of light elements on the sound velocitites in solid iron: implications for the composition of Earth's core. *Earth Planet. Sci. Lett.* **254**, 233–238.

Barin I., Sauert F., Schultze-Rhonhof E. and Sheng W. S. (1989) *Thermochemical Data of Pure Substances, Part I and Part II*. CH Verlagsgesellschaft, Weinheim, Germany.

Birch F. (1952) Elasticity and constitution of the Earth's interior. *J. Geophys. Res.* **57**, 227–286.

Bohlen S. R. and Boettcher A. L. (1982) The quartz coesite transformation: a precise determination and the effects of other components. *J. Geophys. Res.* **87**, 7073–7078.

Bouchard D. and Bale C. W. (1995) Simultaneous-optimization of thermochemical data for liquid-iron alloys containing C, N, Ti, Si, Mn, S, and P. *Metall. Mater. Trans. B Proc. Metall. Mater. Process. Sci.* **26**, 467–484.

Brett R. (1984) Chemical equilibration of the Earth's core and upper mantle. *Geochim. Cosmochim. Acta* **48**, 1183–1188.

Canup R. M. (2004) Origin of terrestrial planets and the Earth–Moon system. *Phys. Today* **57**, 56–62.

Chabot N. L. and Agee C. B. (2003) Core formation in the Earth and Moon: new experimental constraints from V, Cr, and Mn. *Geochim. Cosmochim. Acta* **67**, 2077–2091.

Chabot N. L. and Drake M. J. (1999) Potassium solubility in metal: the effects of composition at 15 kbar and 1900 °C on partitioning between iron alloys and silicate melts. *Earth Planet. Sci. Lett.* **172**, 323–335.

Chipman J. (1955) Atomic interaction in molten alloy steels. *J. Iron Steel Inst.* **180**, 97–106.

Corgne A., Keshav S., Wood B. J., McDonough W. F. and Fei Y. (2008) Metal–silicate partitioning and constraints on core composition and oxygen fugacity during Earth accretion. *Geochim. Cosmochim. Acta* **72**, 574–589.

Corgne A., Siebert J. and Badro J. (2009) Oxygen as a light element: a solution to single-stage core formation. *Earth Planet. Sci. Lett.* **288**, 108–114.

Cottrell E., Walter M. J. and Walker D. (2009) Metal–silicate partitioning of tungsten at high pressure and temperature: implications for equilibrium core formation in Earth. *Earth Planet. Sci. Lett.* **281**, 275–287.

Fitoussi C., Bourdon B., Kleine T., Oberli F. and Reynolds B. C. (2009) Si isotope systematics of meteorties and terrestrial peridotites: implications for Mg/Si fractionation in the solar nebula and for Si in the Earth's core. *Earth Planet. Sci. Lett.* **287**, 77–85.

Georg R. B., Halliday A. N., Schauble E. and Reynolds B. C. (2007) Silicon in the Earth's core. *Nature* **447**, 1102–1106.

Gessmann C. K. and Rubie D. C. (2000) The origin of the depletions of V, Cr and Mn in the mantles of the Earth and Moon. *Earth Planet. Sci. Lett.* **184**, 95–107.

Halliday A. N. and Wood B. J. (2009) How did Earth accrete? *Science* **325**, 44–45.

Holland T. J. B. (1980) The reaction albite = jadeite + quartz determined experimentally in the range 600–1200 °C. *Am. Mineral.* **65**, 129–134.

Kegler P., Holzheid A., Frost D. J., Rubie D. C., Dohmen R. and Palme H. (2008) New Ni and Co metal–silicate partitioning data and their relevance for an early terrestrial magma ocean. *Earth Planet. Sci. Lett.* **268**, 28–40.

Kleine T., Mezger K., Palme H. and Munker C. (2004) The W isotope evolution of the bulk silicate Earth: constraints on the timing and mechanisms of core formation and accretion. *Earth Planet. Sci. Lett.* **228**, 109–123.

Kleine T., Munker C., Mezger K. and Palme H. (2002) Rapid accretion and early core formation on asteroids and the terrestrial planets from Hf–W chronometry. *Nature* **418**, 952–955.

Li J. and Agee C. B. (1996) Geochemistry of mantle–core differentiation at high pressure. *Nature* **381**, 686–689.

Li J. and Agee C. B. (2001) The effect of pressure, temperature, oxygen fugacity and composition on partitioning of nickel and cobalt between liquid Fe–Ni–S alloy and liquid silicate: implications for the Earth's core formation. *Geochim. Cosmochim. Acta* **65**, 1821–1832.

Ma Z. T. (2001) Thermodynamic description for concentrated metallic solutions using interaction parameters. *Metall. Mater. Trans. B Proc. Metall. Mater. Process. Sci.* **32**, 87–103.

McDade P., Wood B. J., Westrenen W. V., Brooker R., Gudmundsson G., Soulard H., Najorka J. and Blundy J. (2002) Pressure corrections for a selection of piston-cylinder cell assemblies. *Mineral. Mag.* **66**, 1021–1028.

McDonough W. F. (2003) Compositional models for the Earth's core. In *The Mantle and Core*, vol. 2 (ed. R. W. Carlson). Elsevier-Pergamon, Oxford, pp. 547–588.

McDonough W. F. and Sun S.-s. (1995) The composition of the Earth. *Chem. Geol.* **120**, 223–253.

O'Neill H. S. C., Berry A. J. and Eggins S. M. (2008) The solubility and oxidation state of tungsten in silicate melts: implications for the comparative chemistry of W and Mo in planetary differentiation processes. *Chem. Geol.* **255**, 346–359.

O'Neill H. S. C. and Eggins S. M. (2002) The effect of melt composition on trace element partitioning: an experimental investigation of the activity coefficients of FeO, NiO, CoO, MoO_2 and MoO_3 in silicate melts. *Chem. Geol.* **186**, 151–181.

Okuchi T. (1997) Hydrogen partitioning into molten iron at high pressure: implications for Earth's core. *Science* **278**, 1781–1784.

Ono-Nakazato H., Taguchi K., Maruo R. and Usui T. (2007) Silicon deoxidation equilibrium of molten Fe–Mo alloy. *ISIJ Int.* **47**, 365–369.

Ozawa H., Hirose K., Mitome M., Bando Y., Sata N. and Ohishi Y. (2008) Chemical equilibrium between ferropericlase and molten iron to 134 GPa and implications for iron content at the bottom of the mantle. *Geophys. Res. Lett.* **35**.

Pahlevan K. and Stevenson D. J. (2007) Equilibration in the aftermath of the lunar-forming giant impact. *Earth Planet. Sci. Lett.* **262**, 438–449.

Presnall D. C., Dixon S. A., Dixon J. R., O'Donnell T. H., Brenner N. L., Schrock R. L. and Dycus D. W. (1978) Liquidus phase relations on the join Diopside–Forsterite–Anorthite from 1 atm to 20 kbar: their bearing on the generatin and crystallization of basaltic magma. *Contrib. Mineral. Petrol.* **66**, 203–220.

Righter K. (2003) Metal–silicate partitioning of siderophile elements and coreformation in the early Earth. *Ann. Rev. Earth Planet. Sci.* **31**, 135–174.

Righter K. and Drake M. J. (1997) Metal–silicate equilibrium in a homogeneously accreting earth: new results for Re. *Earth Planet. Sci. Lett.* **146**, 541–553.

Ringwood A. E. (1966) Chemical evolution of the terrestrial planets. *Geochim. Cosmochim. Acta* **30**, 41–104.

Rubie D. C., Gessmann C. K. and Frost D. J. (2004) Partitioning of oxygen during core formation on the Earth and Mars. *Nature* **429**, 58–61.

Rubie D. C., Melosh H. J., Reid J. E., Liebske C. and Righter K. (2003) Mechanisms of metal–silicate equilibration in the terrestrial magma ocean. *Earth Planet. Sci. Lett.* **205**, 239–255.

Shahar A., Ziegler K., Young E. D., Ricolleau A., Schauble E. and Fei Y. (2009) Experimentally determined Si isotope fractionation between silicate and Fe metal and implications for Earh's core formation. *Earth Planet. Sci. Lett.* **288**, 228–234.

Steelmaking J. S. f. t. P. o. S. a. t. t. C. o. (1988) *Steelmaking Data Sourcebook*. Gordon and Breach, New York.

Stevenson D. J. (1981) Models of the Earth's core. *Science* **214**, 611–619.

Thibault Y. and Walter M. J. (1995) The influence of pressure and temperature on the metal–silicate partition coefficients of nickel and cobalt in a model C1 chondrite and implications for metal segregation in a deep magma ocean. *Geochim. Cosmochim. Acta* **59**, 991.

Touboul M., Kleine T., Bourdon B., Palme H. and Wieler R. (2007) Late formation and prolonged differentiation of the Moon inferred from W isotopes in lunar metals. *Nature* **450**, 1206–1209.

Tronnes R. G. and Frost D. J. (2002) Peridotite melting and mineral–melt partitioning of major and minor elements at 22–24.5 GPa. *Earth Planet. Sci. Lett.* **197**, 117–131.

Wade J. and Wood B. J. (2001) The Earth's 'missing' niobium may be in the core. *Nature* **409**, 75–78.

Wade J. and Wood B. J. (2005) Core formation and the oxidation state of the Earth. *Earth Planet. Sci. Lett.* **236**, 78–95.

Wagner C. (1962) *Thermodynamics of Alloys*. Addison-Wesley, Reading, MA.

Walker D. (1991) Lubrication, gasketing and precision in multianvil experiments. *Am. Mineral.* **76**, 1092–1100.

Walker D., Carpenter M. A. and Hitch C. M. (1990) Some simplifications to multianvil devices for high pressure experiments. *Am. Mineral.* **76**, 1020–1028.

Wood B. J. (1993) Carbon in the core. *Earth Planet. Sci. Lett.* **117**, 593–607.

Wood B. J., Wade J. and Kilburn M. R. (2008) Core formation and the oxidation state of the Earth: additional constraints from Nb, V and Cr partitioning. *Geochim. Cosmochim. Acta* **72**, 1415–1426.

Yagi T., Akaogi M., Shimimura O., Suzuki T. and Akimoto S. (1987) In situ observation of the olivine-spinel phase transformation in Fe_2SiO_4 using synchrotron radiation. *J. Geophys. Res.* **92**, 6207–6213.

Yin Q. Z., Jacobsen S. B., Yamashita K., Blichert-Toft J., Telouk P. and Albarede F. (2002) A short timescale for terrestrial planet formation from Hf–W chronometry of meteorites. *Nature* **418**, 949–952.

Zerr A., Diegeler A. and Boehler R. (1998) Solidus of Earth's deep mantle. *Science* **281**, 243–246.

Zhang J. and Herzberg C. T. (1994) Melting experiments on anhydrous peridotite KLB-1 from 5.0 to 22.5 GPa. *J. Geophys. Res.* **99**, 17729–17742.

Associate editor: F.J. Ryerson